FINAL TECHNICAL REPORT

Agency and Organization:	**University of Utah, Energy and Geoscience Institute**
Recipient Organization:	**University of Wisconsin System**
DUNS Number:	**161202122**
Recipient Address:	**Research and Sponsored Programs** **21 N. Park Street, Suite 6401** **Madison, WI 53715-1218**
Subaward Agreement No.	**10039612-UWM**
Project Title:	**Measuring and Modeling Deformation at a Geothermal Site in Utah Selected for the DOE FORGE Program**
Principal Investigator:	**Kurt Feigl, Professor, feigl@wisc.edu, (608) 262 0176**
Report Submitted by:	**Kurt Feigl, Professor, feigl@wisc.edu, (608) 262 0176**
Reporting Period:	**August 16th, 2018 and July 30th, 2024**
Date of Report Submission:	**July 29th, 2024**
Report Frequency:	**Final**
FORGE PI	**Dr. Joseph Moore**

Signature: Kurt L. Feigl Date 2024/07/29

Table of Contents

Final Report: Measuring and Modeling Deformation at a Geothermal Site in Utah Selected for the DOE FORGE Program

Kurt Feigl and Sam Batzli

1 Abstract

This report describes research activities between August 16th, 2018 and July 30th, 2024 under Subaward Agreement between the University of Utah and the University of Wisconsin System. The goals of the research activities are to conduct: InSAR analysis (Subtask 3.7.3) and Ground Surface Deformation Modeling (Subtask 3.4.4). Interferometric Synthetic Aperture Radar (InSAR) data have been obtained from two satellite missions, combined pair-wise into interferograms to assess ground deformation. The results are registered ("geo-coded") into a cartographic map projection and published on the Geothermal Data Repository. Time series of displacement inferred from InSAR data are compared with those measured by GPS surveying. The InSAR data analyzed here do not show any measurable deformation in the area immediately surrounding the FORGE wells. Nor do the time series of vertical displacement measured by GPS show any signals that would reject the null hypothesis of no internal deformation with 95 percent confidence. No vertical surface displacement that could be measurable by InSAR or GPS is expected from the stimulation experiments conducted at the Utah FORGE site in 2023 or 2024. The expected vertical displacement at the Earth's surface is less than 1 millimeter, based on modeling using an analytic solution (Mogi). Hydromechanical modeling in a poroelastic medium conducted using the finite-element method also indicates vertical surface displacements smaller than 1 millimeter in magnitude. In other words, the magnitude of the deformation produced by injection experiments is too small to be measured by InSAR or GPS. A seismic event with magnitude M ~ 4, however, would likely produce measurable deformation, depending on depth and focal mechanism.

2 Introduction

The scientific rationale and results of the FORGE project are described elsewhere, [e.g., *Simmons et al.*, 2019]. Here we focus on measuring and modeling deformation at the Utah FORGE site (*Figure 1*). The goals of the research activities are to conduct: InSAR analysis (Subtask 3.7.3) and Ground Surface Deformation Modeling (Subtask 3.4.4).

3 InSAR analysis (Subtask 3.7.3)

3.1 Objective from statement of work

Under this subtask, the Recipient is to obtain and interpret Interferometric Synthetic Aperture Radar (InSAR) interferograms to assess ground deformation and to complement continuous GPS monitoring. Additional scenes will be acquired from several satellite missions as available. The new scenes will be compared with previous scenes in interferometrically compatible combinations. The InSAR results will be evaluated to estimate ground deformation. Hydromechanical modeling in a poroelastic medium will be conducted. The InSAR data will be

analyzed and interpreted, and the results registered ("geo-coded") and integrated into the earth model.

3.2 Methodology

To measure deformation at the Utah FORGE site, we use InSAR — Interferometric Synthetic Aperture Radar. We have collected and analyzed SAR data covering the Utah FORGE site (Figure 1), especially FORGE wells 58-32, 68-32, and 78-32 (Table 1). The data sets spanning late 2019 through March 2024 were acquired by two independent satellite missions: TSX and S1.

The TSX data set consists of SAR images acquired by TerraSAR-X and TanDEM-X satellite missions operated by the German Space Agency (DLR). The images acquired on individual dates are listed in *Table 4*. Synthetic Aperture Radar data from the TerraSAR-X and the TanDEM-X satellite missions operated by the German Space Agency (DLR) were used under the terms and conditions of Research Project RES1236. DLR charges a fee of 200 EUR for one scene as the cost of fulfilling user requests (COFUR) under the "general science" category.

Interferometric pairs (interferograms) were created using GMT-SAR processing software [Sandwell et al., 2011]. Software is available publicly on GitHub for the General Inversion of Phase Technique (GIPhT) [*Feigl et al.*, 2019], the PoroTomo project [*Reinisch and Feigl*, 2018], and the UW Madison HTCondor InSAR Workflow [*Reinisch et al.*, 2018a]. We have analyzed TSX data from 2019 through 2024. The interferometric pairs from TSX data are publicly available as data sets on the Geothermal Data Repository:

Utah FORGE InSAR Data from 2020

Utah FORGE InSAR Data from 2021

Utah FORGE InSAR Data from 2022

Utah FORGE: InSAR Data Best Pairs

Utah FORGE: Interferometric Synthetic Aperture Radar Data from 2023 and 2024

The S1 data set includes SAR data from the SENTINEL-1 satellite mission operated by the European Space Agency (ESA). The SENTINEL-1 mission currently includes two spacecraft in orbit: SENTINEL-1A and SENTINEL-1B. These data sets cover the Utah FORGE site from late 2016 through early 2024. The SAR sensor aboard the Sentinel-1B spacecraft did not acquire any InSAR data covering the Utah FORGE site after December 2021. "Sentinel-1B experienced an anomaly which rendered it unable to deliver radar data in December 2021" [*ESA*, 2022] https://www.eoportal.org/satellite-missions/copernicus-sentinel-1]. On the other hand, Sentinel-1A acquired SAR data covering the Utah FORGE site in 2023 and 2024. To analyze the Sentinel data, we use ASF HyP3, the Alaska Satellite Facility's Hybrid Pluggable Processing Pipeline [*ASF*, 2024], which became available as a service in April 2024. The S1 pairs analyzed between 2020 and 2024 are listed in *Table 5* and *Table 6* for Sentinel-1A and Sentinel-1B, respectively.

3.3 Time series analysis

We have calculated many different interferometric pairs. We analyze the interferometric pairs as time series of displacement using the Miami INsar Time-series software in PYthon (MintPy) workflow (Yunjun et al., 2019). The MintPy workflow partially mitigates atmospheric effects and topographic artefacts.

For each data set, we show a graph of the relative positions of TSX/TDX spacecraft at the times that individual SAR images were acquired (circles) as well as the separation ("perpendicular baseline", left-hand scale) between two different positions (at different times) in the orbital trajectory. Each interferometric pair is shown as line segment, colored by average spatial coherence (right hand scale) in a so-called "network diagram" (*Figure 2, Figure 5, Figure 9,* and *Figure 14*).

The quantity of interest is the (scalar) displacement along the radar line of sight (LOS). By convention, positive values of LOS displacement correspond to motion toward the satellite. For example, *Figure 3* shows a sequence of maps of the LOS displacement at dates between 2019 and 2023.

To visualize the deformation field, we consider the mean rate of LOS displacement over the full, multi-year time interval spanned by the data. Each map in *Figure 4*, *Figure 10*, *Figure 12*, *Figure 15*, and *Figure 8* shows the mean rate of LOS displacement averaged over the time interval shown in the network diagram. In each figure, the rate is referred a reference pixel.

3.4 GPS

Here we consider the vertical component of displacement measured by GPS and provided by Ben Erickson:

> Sent: Monday, May 13, 2024 8:47 AM; Subject: Re: GPS Monument Data
>
> I've attached the most recent GPS processing; keep in mind, the comparative initial date has changed from the referenced spreadsheet. I also maintain the Foundry site with this spreadsheet, the comparative time series, and raw GPS data.
>
> Ben Erickson (he/him); Senior Geologist | M.S., P.G

To mitigate the effects of changing reference frames, we analyze the GPS time series of vertical displacement with respect to several different references. This approach would highlight any internal deformation within the GPS network.

Figure 17 shows the relative vertical displacement of each station with respect to the continuously operating station GDM-01. Although there is a suggestion of a seasonal effect (upward displacements during the winter and downward displacements during the summer), there is no significant vertical displacement between the surveys bracketing the date of the flow test in 2023.

Figure 18 shows the vertical displacement of each station referred to the overall mean of all stations. No individual station appears to deviate consistently from the 95-percent confidence interval.

Figure 19 shows the vertical displacement of each station referred to the mean of all stations for each survey. This figure does not show any vertical displacements that would reject the null hypothesis of no deformation with 95% confidence.

3.5 Discussion

The InSAR data do not show any deformation that is obviously associated with FORGE wells 58-32, 68-32, or 78-32, shown as triangles in the figures. The large-scale patterns are probably the result of atmospheric effects that are partially correlated with topography. The wide-scale patterns are probably the result of unmodeled orbital effects in the satellite trajectories. Nor do the time series of vertical displacement measured by GPS show any signals that would reject the null hypothesis of no internal deformation with 95 percent confidence.

4 Ground Surface Deformation Modeling (Subtask 3.4.4).

4.1 Objective from amended statement of work

The Recipient will model ground surface deformation for comparison with InSAR data. The deliverable will be in the form of a report that makes comparison of modeled results with other monitoring techniques used at Utah FORGE such as GPS surveys and strain measurements. It will make reference to analogous injection-production fields elsewhere in the world.

4.2 Analytic modeling configuration

To calculate the order of magnitude of the displacement at the Earth's surface, we performed forward modeling using a simple model [*Mogi*, 1958]. This model assumes an inflating sphere buried in a half space with uniform elastic properties. The Mogi model expresses vertical displacement u_z of a point on the ground in terms of the volume change ΔV and depth d of a subsurface source, as shown in the following equation from [*Segall*, 2010].

$$u_z = \frac{(1-\nu)\Delta V}{\pi} \frac{d}{(\rho^2 + d^2)^{3/2}},$$

where ΔV is the injected volume, u_z is vertical displacement, ν is Poisson's ratio (here assumed to be ¼), d is depth, and ρ is radial horizontal distance from center of source to observation point [*Segall*, 2010]. Vertical displacement u_z is a linear function of the volume ΔV injected at depth. In contrast, displacement u_z is a non-linear function of depth d.

For simplicity, we use an (X,Y) coordinate system with an origin centered on the toe of Well 16A(78)-32. To estimate the depth of the volume change, we followed the document entitled *End of Job Report Hydraulic Fracturing of Well 16A(78)-32 (April 2022)* prepared by Kevin England and John McLennan which reports the following information.

> "The bit was run to near the end of the open-hole section of the wellbore (10,951 ft MD) while the casing scraper reached a depth of 10,761.62 ft MD within the cased-hole and ensured the absence of debris. The drift sub was run one joint above the casing scraper and reached a depth of 10,726.07 ft MD which assured that there is adequate clearance to run the bridge plug to the maximum planned depth of 10,670 ft MD.

> There were some tight spots in the open-hole (~10,857 – 10,872 ft MD) which were worked through with the bit by rotation and washing down." [*McLennan*, 2022].

To estimate the total volume for the 2023 and 2024 tests at the Utah FORGE site, we considered the details described in the following two sub-sections.

4.2.1 Modeling details - 2023

For the 2023 circulation tests, we follow Munday et al. (2024):

> Two sets of circulation tests were performed in July 2023 to test connectivity between wells 16A and 16B. A comprehensive analysis of the circulation tests is given by Xing et. al. (2024). In this work we use pressure and mass data from the second set of circulation tests performed on July 18 and 19 to fit our THM model. Wellhead pressure, injection rate, and producing rate for the July 18 and 19 tests are given in Figure 3. The injection rates range from 2.5 to 7.5 bpm with a maximum pressure of 4500 psi during the July 18 circulation test. Injection well 16A contains three frac stages spaced approximately 300 feet apart where the bottom stage 1 is 200 ft of open hole at a depth of 10938 ft and stages 2 and 3 are cased and perforated. The flow rate for the July 18 and 19 The flow is partitioned between the three stages and the open hole stage 1 zone receives approximately 50% of the flow for the July 19 tests (Xing et al, 2023).

We calculated the total volume of injected fluid by visually estimating the mean flow rate at approximately 5 barrels per minute and then integrating with respect to time over the 4-hour duration for each of the two tests, as shown in *Figure 21*. Assuming that a barrel is 0.159 m^3, we find a total change in volume of ΔV = 382 m^3 for the circulation tests in 2023.

4.2.2 Modeling details - 2024

For the 2024 test, we refer to the following message from Kevin England, dated May 9, 2024:

> Subject: Fluid volumes pumped into well 16A(78)-32 during the frac stimulation treatments Please see below the actual volumes of fluid that were pumped for each of the frac stages in well 16A. We just received all of the data files from Calfrac and I will confirm all of this in the next few days. I'm pretty sure there is additional volume pumped in stage 6R after we perforated an additional 3 ft of zone (probably close to 3,000 bbl). The total fluid injected is 110,776 bbl (4,652,592 gal).

Assuming that a barrel is 0.159 m^3, we find a total change in volume of ΔV = 18,000 m^3 for the stimulation treatments in 2024.

4.3 Analytic modeling results

We consider six different cases, as listed in Table 2.

The first two cases approximate the stimulations in July 2023 and April 2024, respectively. As shown by solid curves in *Figure 20*, the simulated ground motion forms small bulge of uplift. The maximum values of vertical displacement are 8 micrometer and 4 micrometer, respectively. These values are considerably smaller than the detection limit of 10 millimeters for InSAR.

We also consider three hypothetical cases with large modeled injection volumes (dotted curves). In Case 3, the vertical displacement u_z of 8 mm approaches the detection limit of 10 mm. Cases 4 and 5 consider injection volumes of the same order of magnitude (in absolute value) of the annual rate of net production at a commercial operation. For context, pumping at 500 GPM for 1 year is approximately equivalent to $\Delta V \sim 10^6$ m^3. The values of u_z in Cases 4 and 5 are 80 mm and 800 mm, respectively. In other words, if injection at the same rate as during the 2023 FORGE tests were to continue for a year, then the surface displacement would be measurable by InSAR.

The deformation in Case 4 is similar to that observed at East Mesa in California [*Eneva et al.*, 2012; *Han et al.*, 2011; *Massonnet et al.*, 1997; 1998; *Taylor et al.*, 2013].

To illustrate the non-linear trade-off between depth d and volume change ΔV, we consider another hypothetical case (numbered 6) with a shallow depth d = 500 m and ΔV = 18,000 m^3 (just as in Case 2). Case 6 would produce 20 mm of vertical displacement at the surface (dark blue dotted curve).

4.4 Simulating vertical displacements using the Finite Element Method

To confirm the order of magnitude of the surface deformation expected from the stimulation experiments in July 2023 and April 2024, we apply the finite element method (FEM) to perform numerical simulations. The FEM model applies the poroelastic theory of Biot as implemented using COMSOL Multiphysics [*COMSOL*, 2024b]. This approach has been validated against the analytic solution of Terzhagi [*COMSOL*, 2024a].

In particular, we use a model developed by Larry Murdoch as Milestone 5.1 of FORGE Project 3-2514. The following description is adapted from e-mail communications with Murdoch. As shown in Figure 22, the mesh for the FEM model is symmetric about the left side. The simulated region is below the dark grey patch on the left side. This simulation treats the fracture as a permeable layer that is inflated by injecting fluid. The modulus of the layer currently is small, which would represent an open fracture, like a Mode I fracture.

This model does not include the non-linear effects related to propagation, so it cannot match the pressure history (pressure increases early and then decreases). However, it should be able to match the maximum pressure and injected volume, and the length and orientation of the fracture can be adjusted based on the microseismic interpretations. That should allow the model to predict the magnitudes and patterns of the far field deformation fairly well.

Figure 23 shows the vertical component of displacement along a profile from the center of the field to the eastern side. Each curve shows the displacement accumulated at a time step ranging from the start of injection to a time some 2.5 hours later. The maximum displacement is less than 11 micrometers, the same order of magnitude as calculated using the analytic model. *Figure 24* shows the vertical displacement field in map view.

5 Conclusions

In summary, the InSAR data analyzed do not show any measurable deformation in the area immediately surrounding the FORGE wells. Nor do the time series of vertical displacement measured by GPS show any signals that would reject the null hypothesis of no internal deformation with 95 percent confidence.

No deformation larger than 1 millimeter is expected from the stimulation experiments. This result is not surprising since the stimulation experiments injected relatively small volumes at depths on the order of ~2000 m. The expected deformation is less than 1 mm, i.e., based on the modeling using both an analytic solution (Mogi) and the finite element method. In other words, the magnitude of the deformation produced by injection experiments is too small to be measured by

InSAR. A seismic event with magnitude M ~ 4, however, would likely produce measurable deformation, depending on depth and focal mechanism.

6 Acknowledgments

Interferograms were created using GMT-SAR processing software [*Sandwell et al.*, 2011]. Several figures were created using the Generic Mapping Tools [*Wessel et al.*, 2013].

Software is available publicly on GitHub for the General Inversion of Phase Technique (GIPhT) [*Kurt L. Feigl et al.*, 2019] and the FringeFlow workflow for generating interferometric fringe patterns from synthetic aperture radar data, both developed at UW Madison [*K. L. Feigl et al.*, 2022].

Synthetic Aperture Radar data from the TerraSAR-X and the TanDEM-X satellite missions operated by the German Space Agency (DLR) were used under the terms and conditions of Research Project RES1236.

We gratefully acknowledge support from the Weeks family to the Department of Geoscience at the University of Wisconsin-Madison.

7 References Cited

ASF (2024), ASF HyP3: Alaska Satellite Facility's Hybrid Pluggable Processing Pipeline, edited.

COMSOL (2024a), Biot PoroelasticityRep.

COMSOL (2024b), COMSOL Multiphysics®: The Platform for Physics-Based Modeling and Simulation, edited.

Eneva, M., D. Adams, G. Falorni, and J. Morgan (2012), Surface Deformation in Imperial Valley, CA, From Satellite Radar Interferometry, paper presented at Geothermal Research Council Transactions.

ESA (2022), ESA - Mission ends for Copernicus Sentinel-1B satellite, edited.

Feigl, K. L., S. Batzli, N. Bearson, and E. C. Reinisch (2022), FringeFlow: Workflow for generating interferometric fringe patterns from synthetic aperture radar data, edited.

Feigl, K. L., C. Thurber, L. Powell, P. Sobol, A. Masters, E. C. Reinisch, and S. T. Ali (2019), General Inversion of Phase Technique (GIPhT) software repository, edited.

Han, J.-Y., R. R. Forster, D. E. Moser, A. L. J. Ford, J. Ramirez-Hernandez, and K. F. Tiampo (2011), The spatial and temporal subsidence variability of the East Mesa Geothermal Field, California, USA, and its potential impact on the All American Canal System, International Journal of Remote Sensing, 32(12), 3427-3449, doi:10.1080/01431161003749444.

Massonnet, D., T. Holzer, and H. Vadon (1997), Land subsidence caused by the East Mesa geothermal field, California, observed using SAR interferometry, Geophys. Res. Lett., 24, 901-904.

Massonnet, D., T. Holzer, and H. Vadon (1998), Correction to "Land subsidence caused by the East Mesa geothermal field, California, observed using SAR interferometry", Geophys. Res. Lett., 25(16), 3213-3213.

McLennan, J. (2022), Utah FORGE Well 16A(78)-32 Stimulation Data (April, 2022), edited, Energy and Geoscience Institute at the University of Utah, doi:10.15121/1871203.

Mogi, K. (1958), Relations between the eruption of various volcanoes and the deformations of the ground surfaces around them, Bull. Earthquake Research Institute, 36, 99-134.

Munday, L. B., and R. K. Podgorney (2024), Numerically Testing Conceptual Models of the Utah FORGE Reservoir Using July 2023 Circulation Test Data, United States, 2024-02-27.

Sandwell, D., R. Mellors, X. Tong, M. Wei, and P. Wessel (2011), Open radar interferometry software for mapping surface deformation, Eos, Transactions American Geophysical Union, 92(28), 234-234, doi:10.1029/2011eo280002.

Segall, P. (2010), Earthquake and volcano deformation, 432 pp., Princeton University Press, Princeton, N.J.

Simmons, S. F., et al. (2019), Update on the Geoscientific Understanding of the Utah FORGE Site, paper presented at PROCEEDINGS, 44th Workshop on Geothermal Reservoir Engineering, Stanford University, Stanford, California, February 11-13, 2019.

Taylor, H., M. E. Pritchard, and R. B. Lohman (2013), Recent Changes in Ground Deformation at the East Mesa Geothermal Field, California as Measured by InSAR, AGU Fall Meeting Abstracts, 33, 06.

Wessel, P., W. H. F. Smith, R. Scharroo, J. Luis, and F. Wobbe (2013), Generic Mapping Tools (GMT), edited.

Xing, P., K. England, J. Moore, R. Podgorney, and J. McLennan (2024), Analysis of Circulation Tests and Well Connections at Utah FORGE, paper presented at PROCEEDINGS, 49th Workshop on Geothermal Reservoir Engineering Stanford University, SGP-TR-227, Stanford, California, February 12-14, 2024.

8 Figures

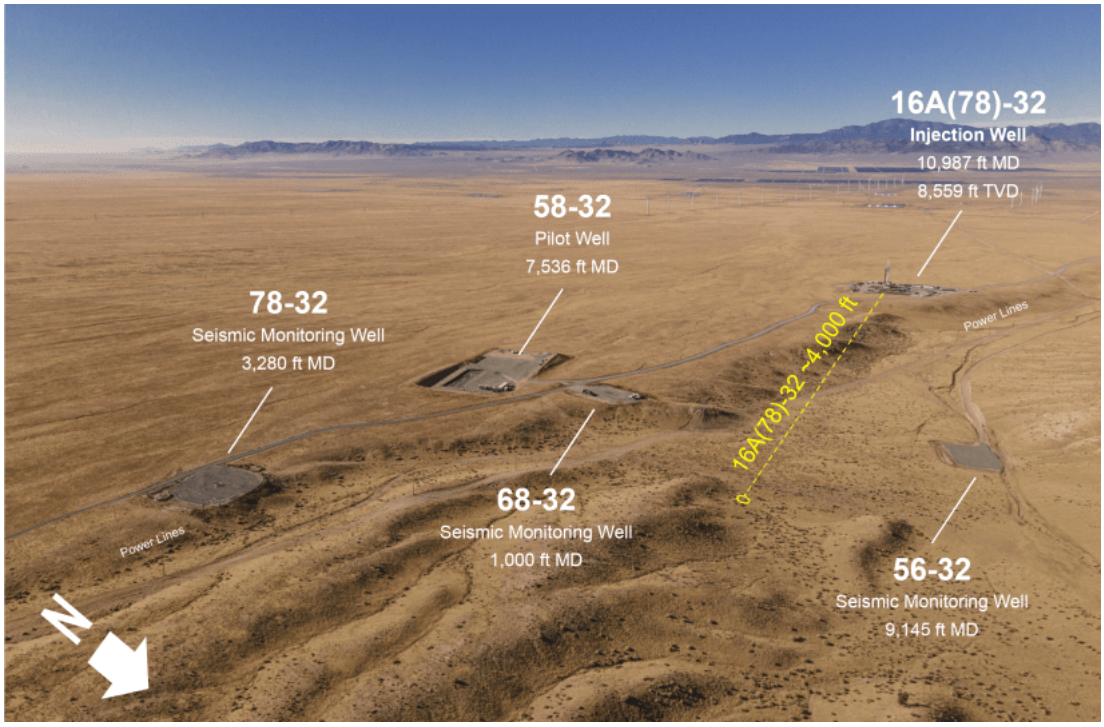

Figure 1. West-southwest facing view of the Utah FORGE site in late 2020, showing drill pads, wells, power line supply, and site access. Well 58-32 is the deep pilot well that can be used to deploy downhole instruments during 2021 stimulations; the bottom 200 feet of the hole are open and the rest is lined with 7-inch casing. Well 68-32 is dedicated to seismic monitoring with a permanently installed geophone and accelerometer at depths of 921-925 ft. Well 78-32 is instrumented with a Silixa DAS cable including a Constellation fiber cemented in the annulus of the 5 ½" casing to 3268 ft; downhole instruments can be deployed in the casing. Well 56-32 has been drilled to 9,145 feet depth, and it is lined with 5½" casing to the toe; this well is also available for deployment of downhole instruments. Figure and caption [https://utahforge.com/site-operations/].

Table 1. Final coordinates of wells, downloaded from Hardwick, Christian. 2020. "Utah FORGE: Updated Phase 2C Well Location Coordinates". United States. https://gdr.openei.org/submissions/1268. File name is "Updated Utah FORGE Phase 2C Well Location"

Well	Latitude (deg)	Longitude (deg)	UTM Northing (m)	UTM Easting (m)	Elevation (m)	h_prec (m)	z_std (m)
58-32	38.500536	-112.887016	4263037.084	335451.380	1684.801	0.100	0.038
68-32	38.501553	-112.886647	4263155.286	335485.169	1685.667	0.100	0.030
78-32	38.500147	-112.883224	4262993.139	335780.484	1701.919	0.100	0.031

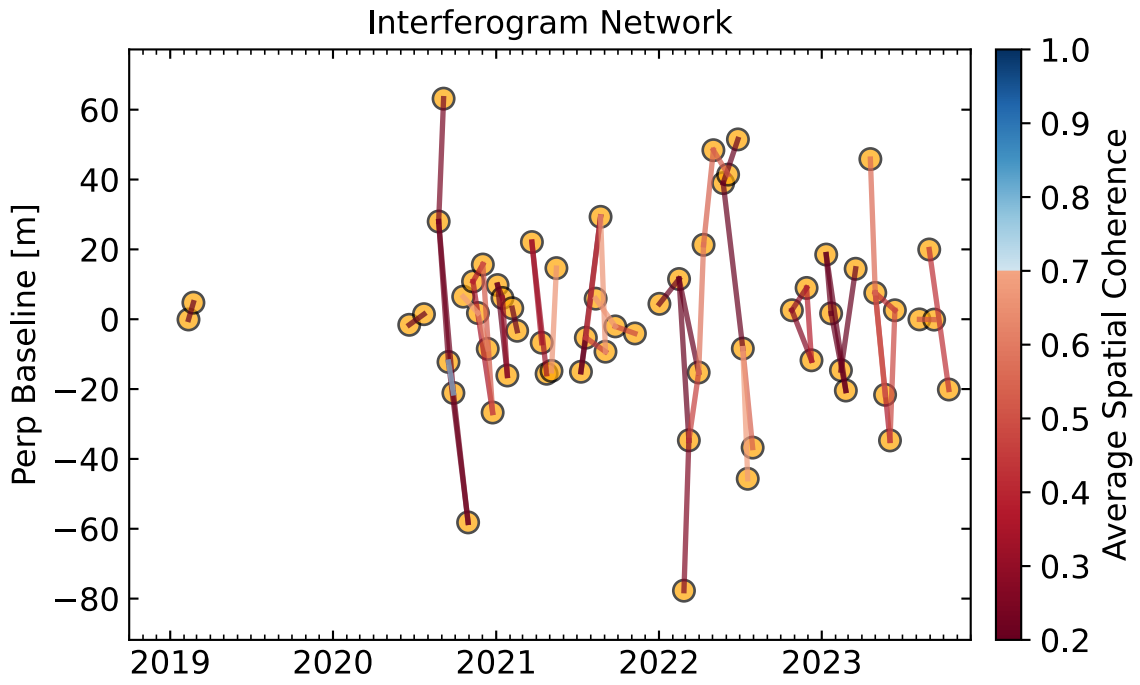

Figure 2. Plot of relative positions of TSX/TDX spacecraft at the times that individual SAR images were acquired in (descending) Track 30 (circles) as well as the orbital separation ("perpendicular baseline", left-hand scale) between two positions forming an interferometric pair (line segments, colored by average spatial coherence (right hand scale). smb://research.drive.wisc.edu/feigl/insar /FORGE/TSX/T30 /feigl_20231222/MINTPY/pic/network.pdf

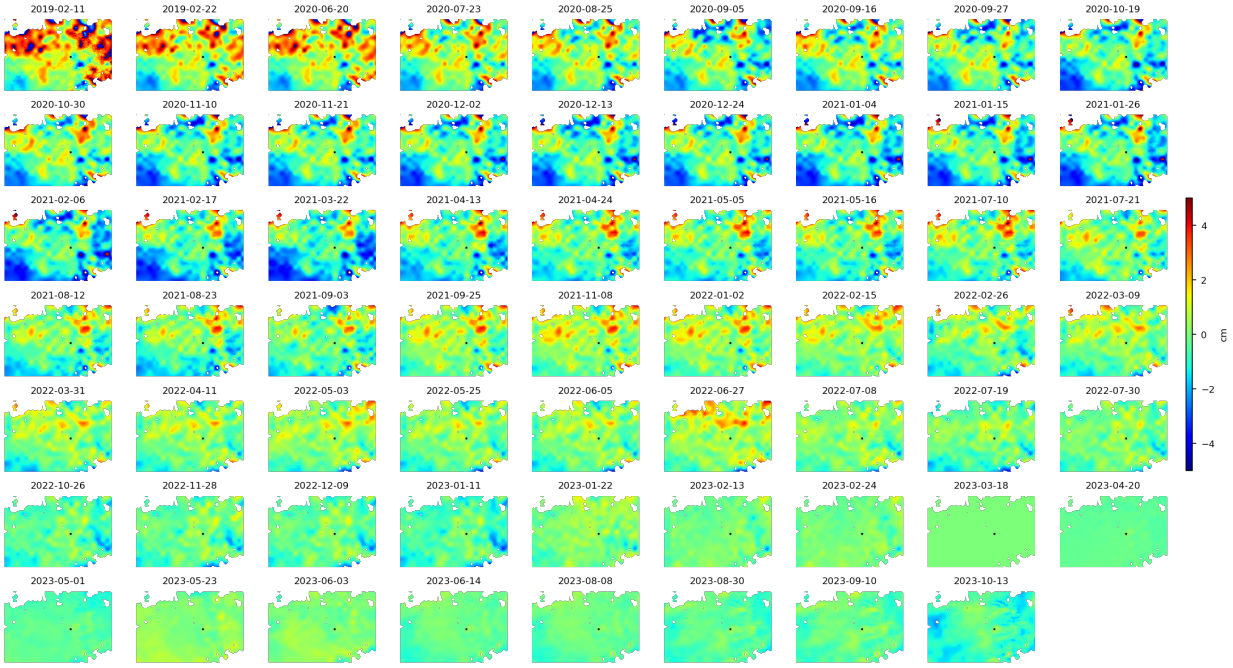

Figure 3. Map of LOS displacement at the dates shown in the previous figure, after accounting for the atmospheric effects and topographic artefacts. Black square indicates the reference location where rate of LOS displacement is zero. In each panel, the black square indicates the reference location where rate of LOS displacement is zero. The spatial extent of each panel matches that shown in the following figure. [smb://research.drive.wisc.edu/feigl/insar/FORGE/TSX /T30/feigl_20231222/MINTPY/pic/timeseries_tropHgt_demErr_wrap10.png]

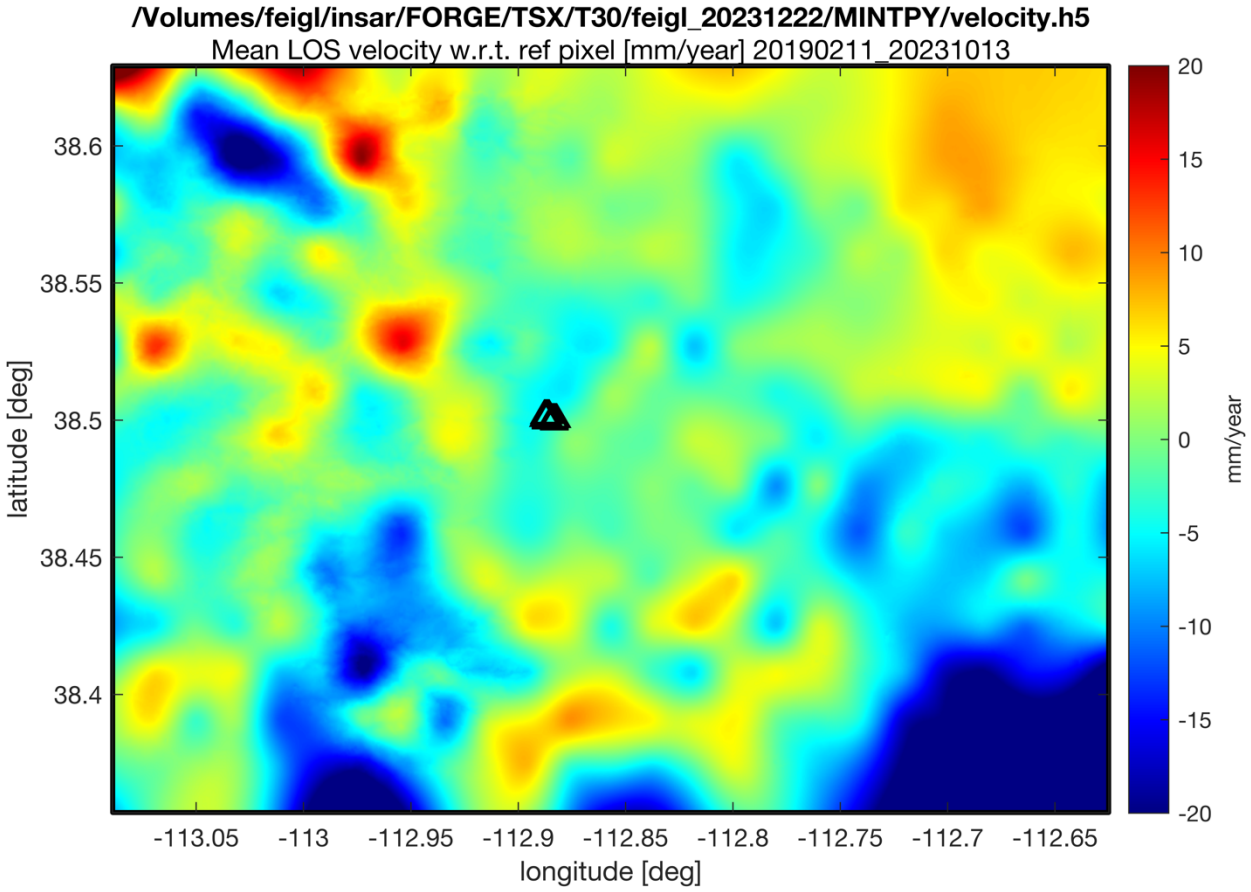

Figure 4. Map of mean rate of LOS displacement averaged over the time interval [2019/02/11 through 2023/10/13]. Coordinates are longitude and longitude in degrees, respectively. Triangles indicate locations of wells 58-32, 68-32, and 78-32. smb://research.drive.wisc.edu/feigl/insar/FORGE/TSX/T30/feigl_20231222/MINTPY/pic/avgPhaseVelocity.png

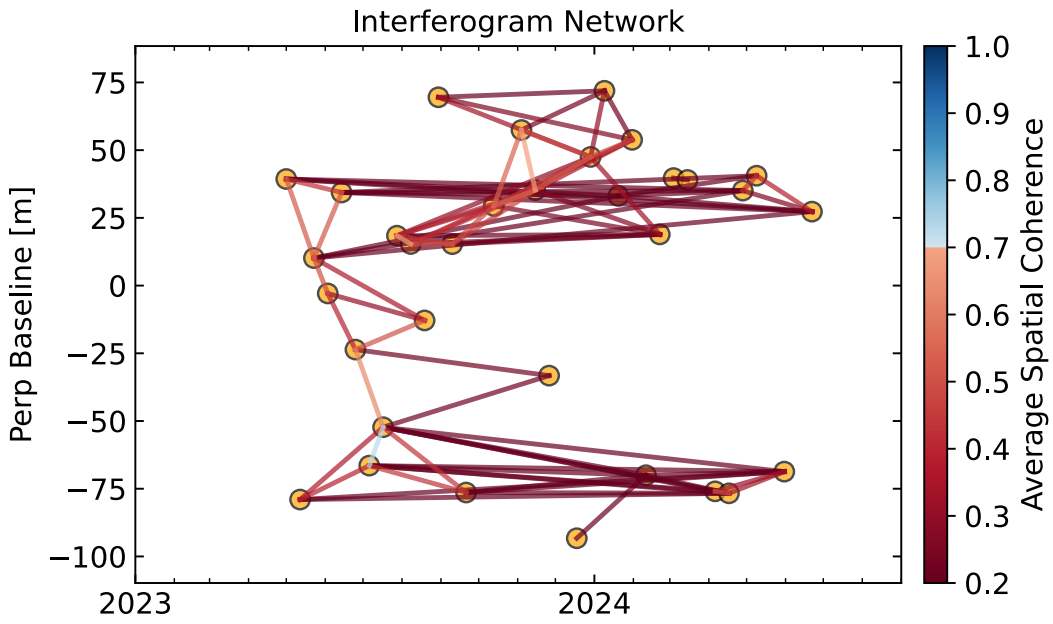

Figure 5. Plot of relative positions of TerraSAR-X and TANDEM-X spacecraft at the times that individual SAR images were acquired (circles) as well as the orbital separation (left-hand scale) between two positions forming an interferometric pair (line segments, colored by average spatial coherence (right hand scale). smb://research.drive.wisc.edu/feigl/insar/ FORGE/TSX/T30/forge_2024/MINTPY6/pic/network.pdf

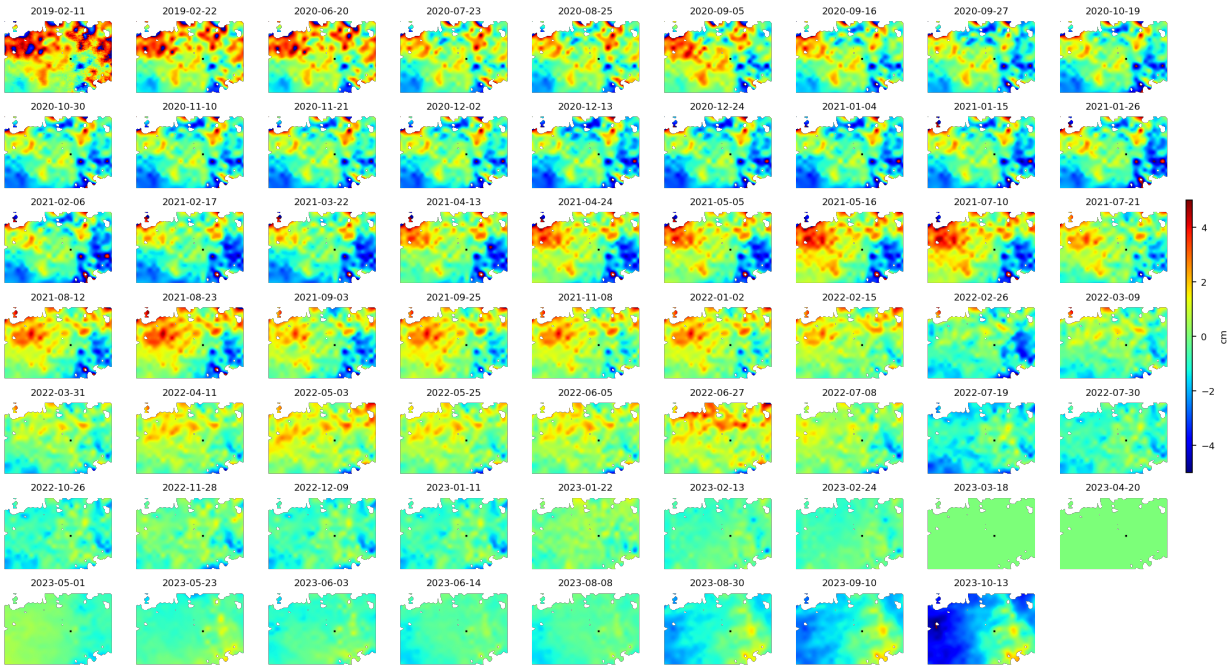

Figure 6. Map of LOS displacement at the dates shown in the previous figure, after accounting for atmospheric effects and topographic artefacts. Black square indicates the reference location where rate of LOS displacement is zero. In each panel, the black square indicates the reference location where rate of LOS displacement is zero. The spatial extent of each panel matches that shown in the following figure. [smb://research.drive.wisc.edu/feigl/insar/FORGE/TSX/T30/ forge_2024/MINTPY6/pic/timeseries_tropHgt_demErr_wrap10.png]

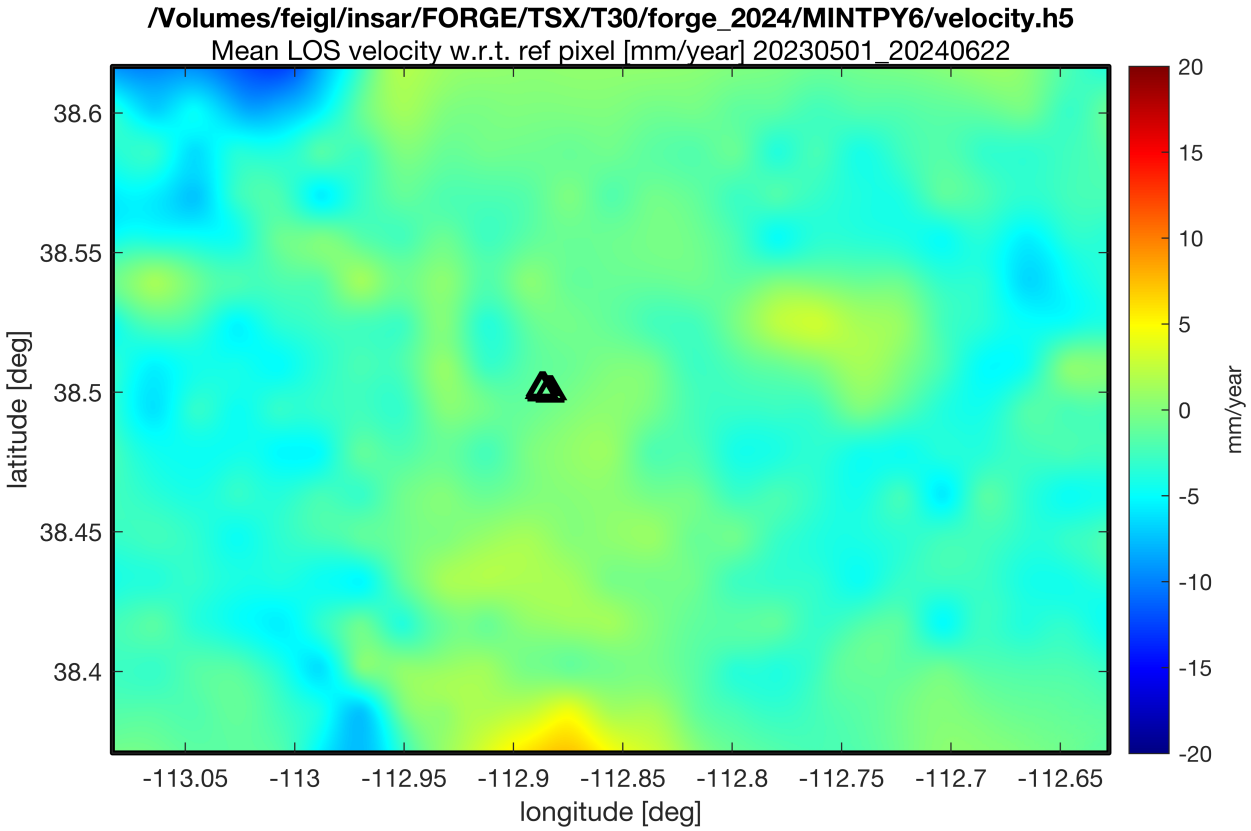

Figure 7. Map of mean rate of LOS displacement averaged over the time interval from 2023/05/01 through 2024/06/22 X and Y coordinates are longitude and longitude in degrees, respectively. Negative values of LOS displacement rate indicate motion away from the satellite. Triangles indicate locations of wells 58-32, 68-32, and 78-32. smb://research.drive.wisc.edu/feigl /insar/FORGE/TSX/T30/ forge_2024/MINTPY6/velocitymapv2_1_velocity.png

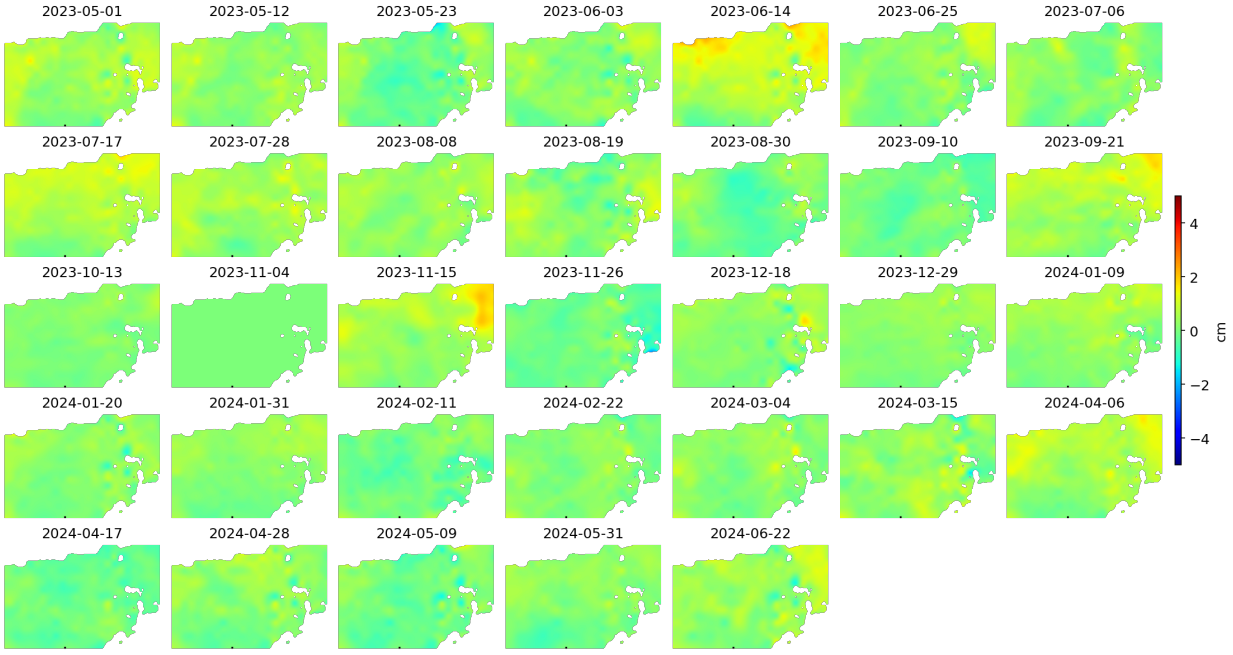

Figure 8. Time series of LOS displacement maps.. Black square indicates the reference location where rate of LOS displacement is zero. The spatial extent of each panel matches that shown in the previous figure.

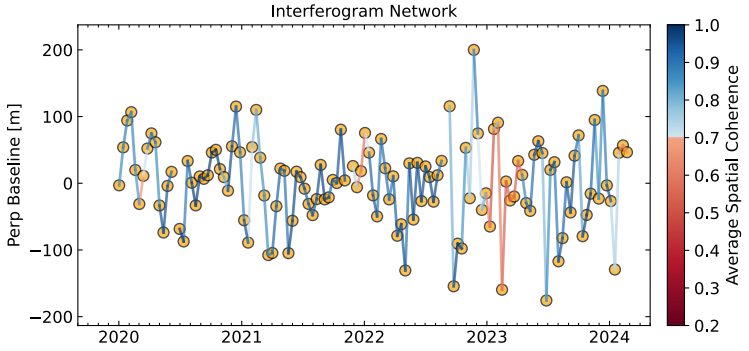

Figure 9. Plot of relative positions of Sentinel 1-A and Sentinel 1-B spacecraft at the times that individual SAR images were acquired (circles) as well as the orbital separation (left-hand scale) between two positions forming an interferometric pair (line segments, colored by average spatial coherence (right hand scale). smb://research.drive.wisc.edu/feigl/insar/ FORGE/SDK/FORGE_DESCENDING2/pic/network.pdf

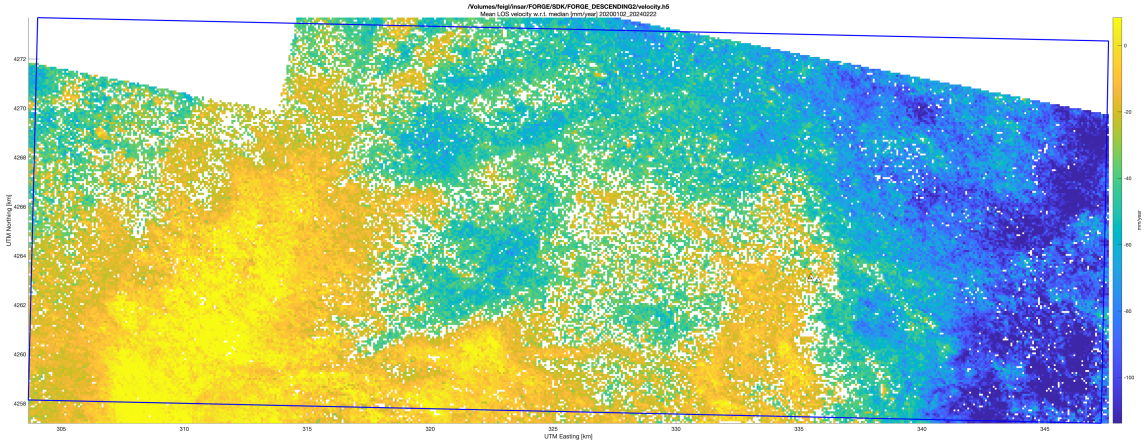

Figure 10. Map of mean rate of LOS displacement averaged over the time interval shown in previous figure, displayed with respect to its median value. X and Y coordinates are UTM easting and northing in km, respectively. Triangles near (E,N) = (335,4263) km indicate locations of wells 58-32, 68-32, and 78-32. Pixels with LOS displacement rates that less than twice their estimated standard deviation in absolute value are not shown. Blue trapezoid indicates bounding box of study area.

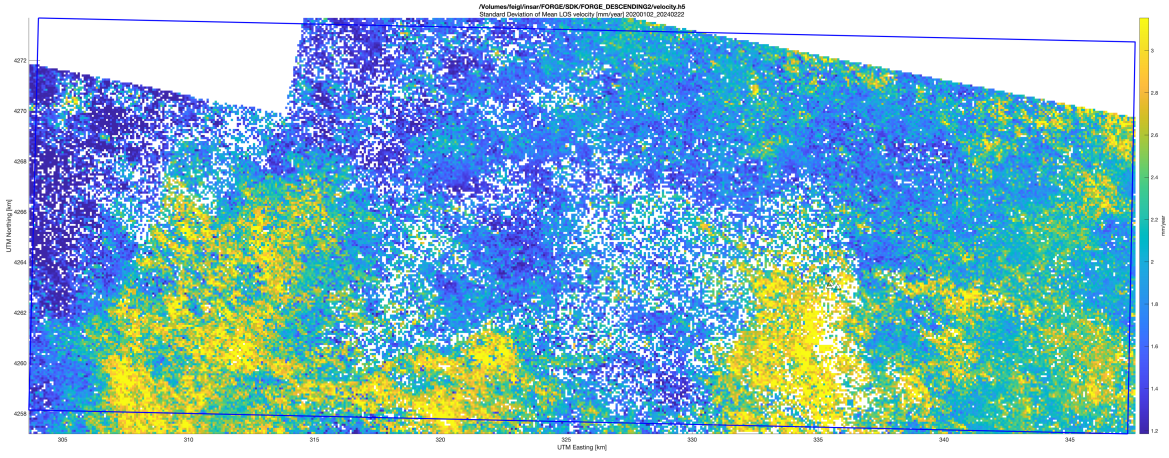

Figure 11. Map of estimated standard deviation of the mean rate of LOS displacement averaged over the time interval shown in previous figure. Plotting conventions as in previous figure.

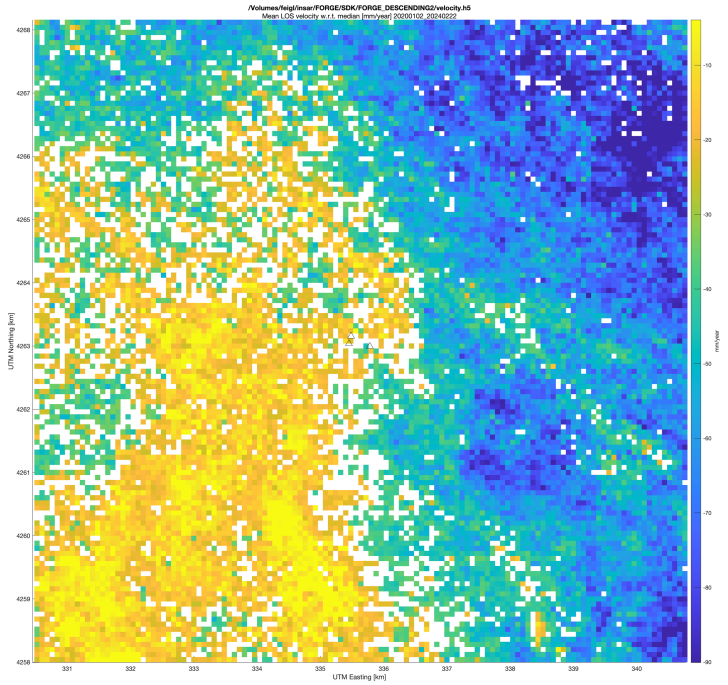

Figure 12. Enlarged map of mean rate of LOS displacement averaged over the time interval shown in previous figure, displayed with respect to its median value. X and Y coordinates are UTM easting and northing in km, respectively. Triangles near (E,N) = (335,4263) km indicate locations of wells 58-32, 68-32, and 78-32. Pixels are approximately 80 m by 80 m. Pixels with LOS displacement rates that less than twice their estimated standard deviation in absolute value are not shown.

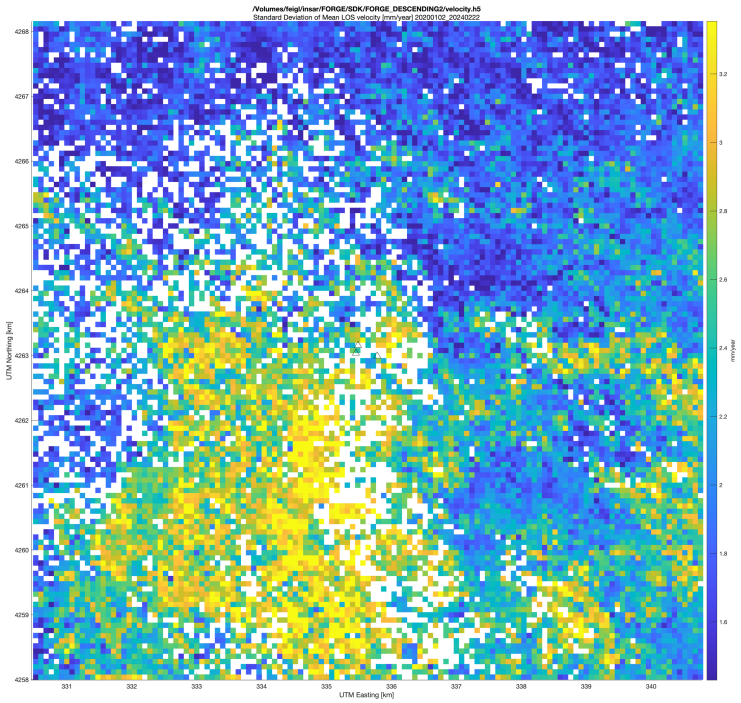

Figure 13. Enlarged map of estimated standard deviation of the mean rate of LOS displacement averaged over the time interval shown in previous figure. Plotting convention as in previous figure.

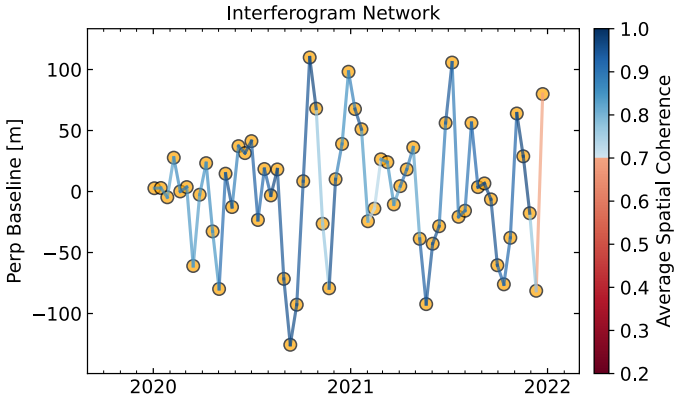

Figure 14. Plot of relative positions of Sentinel-1A spacecraft at the times that individual SAR images were acquired (circles) as well as the orbital separation ("perpendicular baseline", left-hand scale) between two positions forming an interferometric pair (line segments, colored by average spatial coherence (right hand scale). smb://research.drive.wisc.edu/feigl/insar/FORGE/SDK/FORGE_ASCENDING/pic/network.pdf

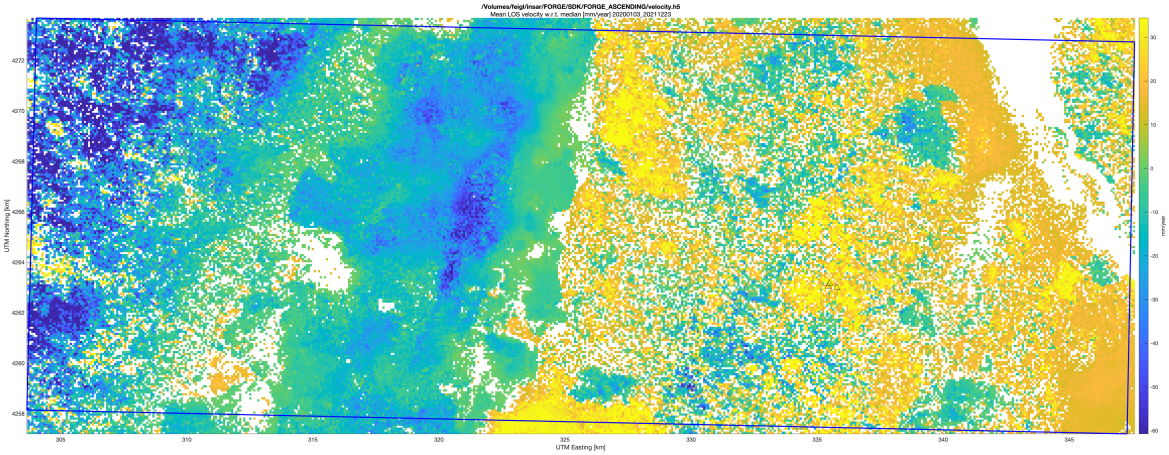

Figure 15. Map of mean rate of LOS displacement averaged over the time interval shown in previous figure, displayed with respect to its median value. X and Y coordinates are UTM easting and northing in km, respectively. Triangles indicate locations of wells 58-32, 68-32, and 78-32. Pixels are approximately 80 m by 80 m. Pixels with LOS displacement rates that less than twice their estimated standard deviation in absolute value are not shown. Blue trapezoid indicates bounding box of study area.

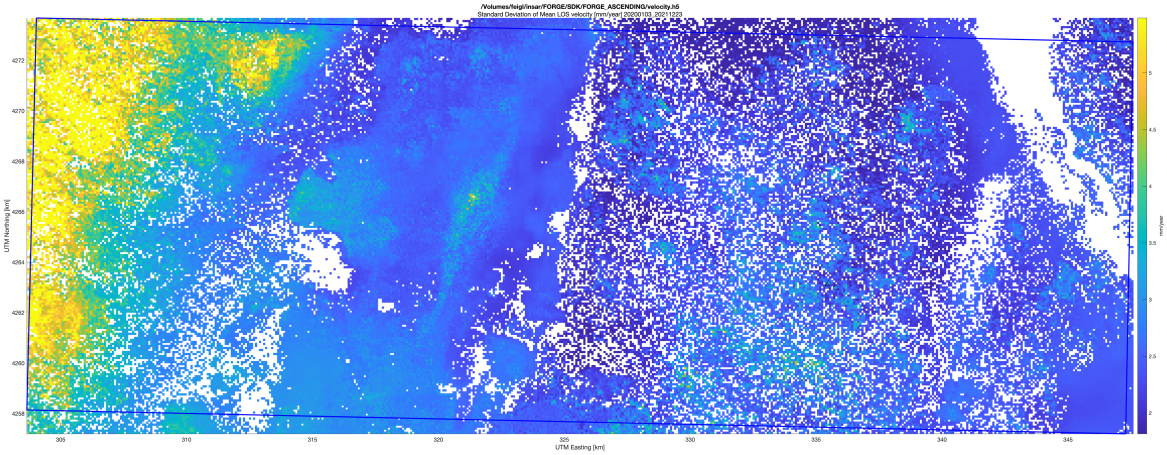

Figure 16. Map of estimated standard deviation of the mean rate of LOS displacement averaged over the time interval shown in previous figure. Plotting convention as in previous figure.

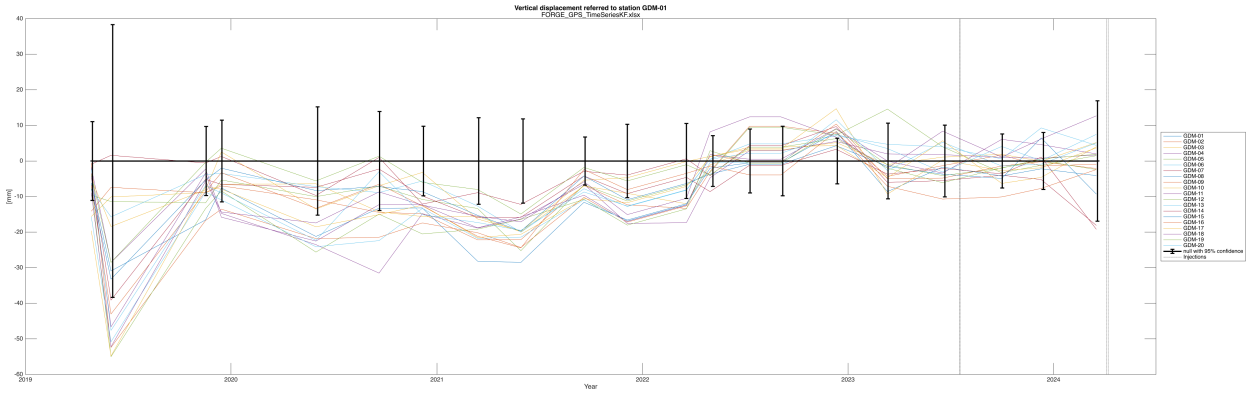

Figure 17. Time series of relative vertical displacements referred to station GDM-01. Error bars delimit ± 2 standard deviations, i.e. 95 percent confidence. Vertical dashed lines indicate tests in July 2023 and April 2024.

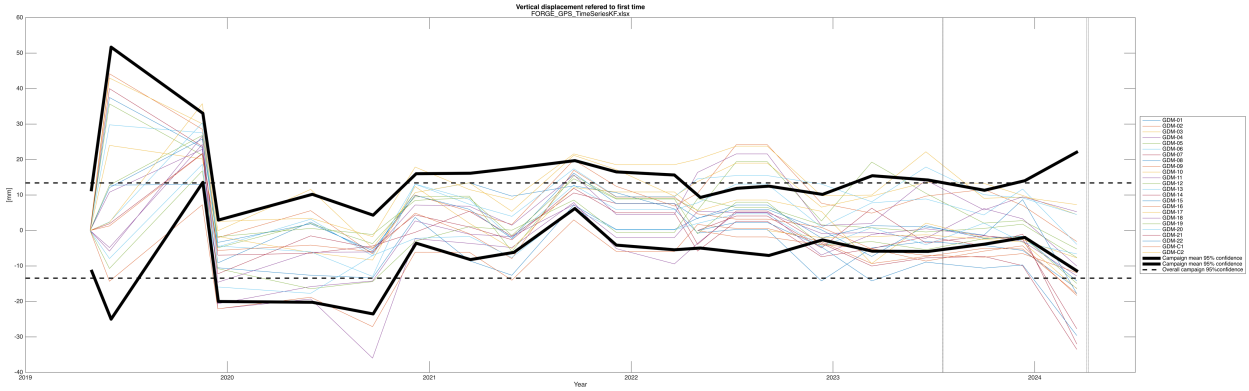

Figure 18. Time series of vertical displacements referred to the initial position of each station at the time of the first survey. Thick black lines delimits interval of 95% confidence about the mean for each campaign. Vertical dashed lines indicate tests in July 2023 and April 2024.

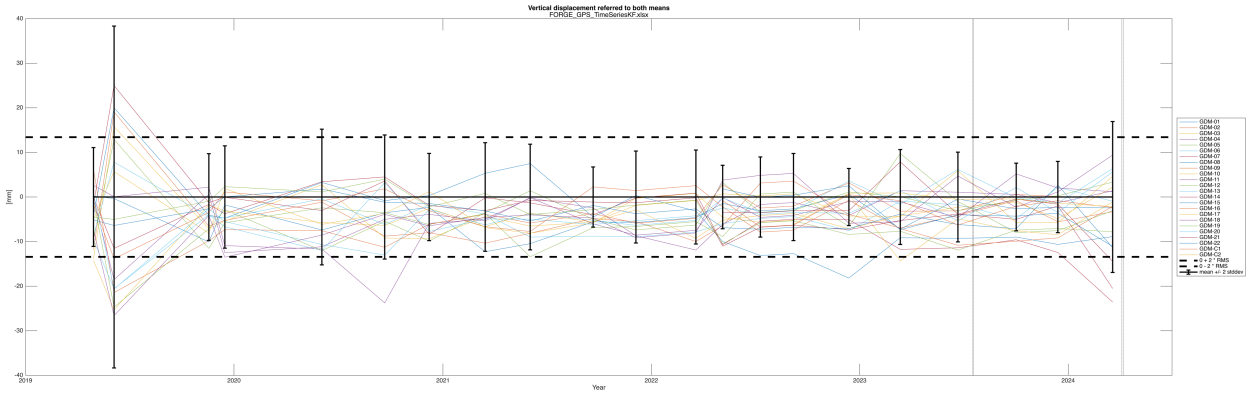

Figure 19. Time series of vertical displacements referred to both the mean of the campaign and the mean for each station.Thick black lines delimits interval of 95% confidence about the mean for each campaign. Vertical dashed lines indicate tests in July 2023 and April 2024.

Table 2. Values of parameters in Mogi model

Case	depth (meter)	Volume Change (cubic meter)	Equivalent seismic moment M_0 [N.m]*	Equivalent seismic magnitude Mw
case = 1	depth = 3334 m	DV = 3.8E+02 m^3	M0 = 1.1E+13 N.m	Mw = 2.7
case = 2	depth = 3334 m	DV = 1.8E+04 m^3	M0 = 5.3E+14 N.m	Mw = 3.8
case = 3	depth = 3334 m	DV = 3.8E+05 m^3	M0 = 1.1E+16 N.m	Mw = 4.7
case = 4	depth = 3334 m	DV = 3.8E+06 m^3	M0 = 1.1E+17 N.m	Mw = 5.3
case = 5	depth = 3334 m	DV = 3.8E+07 m^3	M0 = 1.1E+18 N.m	Mw = 6.0
case = 6	depth = 500 m	DV = 1.8E+04 m^3	M0 = 5.3E+14 N.m	Mw = 3.8

** assuming geometric potency (slip x area) equal to volume change ΔV and shear modulus of 30 GPa.*

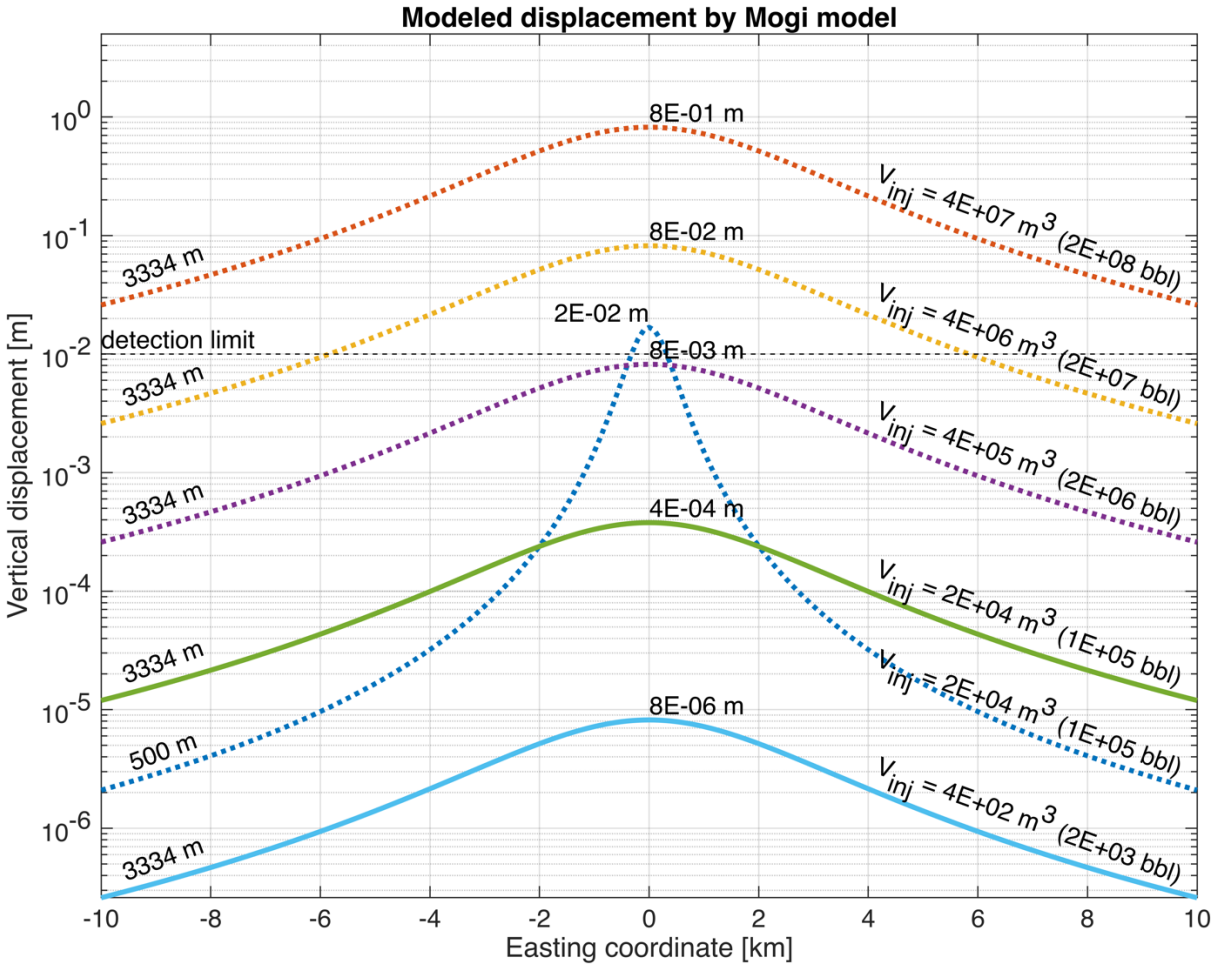

Figure 20. Plot of vertical displacement in meters calculated from the Mogi model for injected volumes approximating the stimulations in July 2023 (light blue solid line) and April 2024 (green solid line) as well as three hypothetical cases (purple, yellow, red) with different values of volume change (labels on right hand side). The dark blue curve shows a hypothetical case with a shallow depth (labels at left).

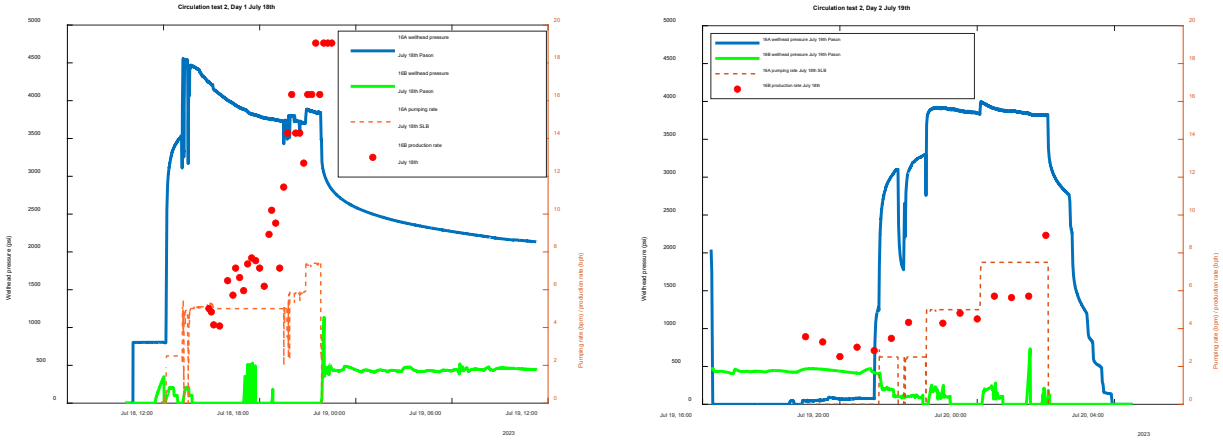

Figure 21. Circulation test 2 data showing wellhead pressure, injection rate, and producing rate for (a) July 18 and (b) July 19, 2023 (after Figure 5 in [Xing et al., 2024]). Figure and caption [Munday and Podgorney, 2024].

Table 3 Input parameters for finite-element modeling using COMSOL from L. Murdoch.

parameter	symbol	values		
fluid density	rhof	000 [kg/m^3]		
length of screened interval in well	screen_len	10 [m]		
radius of well	well_radius	0.1 [m]		
pumping rate	pumping_rate	3E-4[m^3/s]		
gravitational acceleration	g	9.81[m/s^2]		
fracture thickness	frx_thickness	0.1 [m]		
fracture depth	frx_depth	50 [m]		
fracture dip	frx_dip	90 [m]		
property	symbol	granite	alluvium	fracture
Young's modulus	E	1E8[Pa]	1E8[Pa]	1[Pa]
permeability	k	1e-12[m^2]	1e-12[m^2]	1.5E-12[m^2]
storage (effective)	Se	1.00E-07	1.00E-07	1.00E-09
porosity	porosity	0.2	0.2	0.5
Biot coefficient	b_alpha	0.95	0.95	0.9

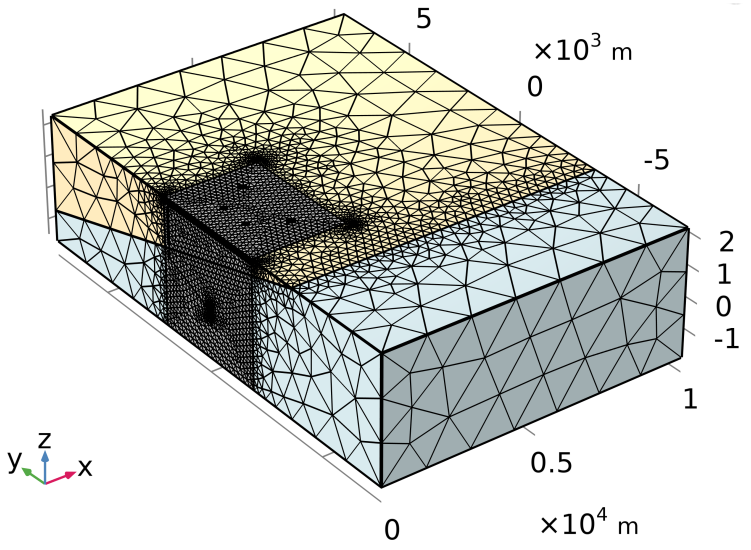

Figure 22. Block diagram for configuration of the finite element model. The model domain is symmetric about the left side and the simulated region is below the dark grey patch on the left side. The eastward X axis points toward the upper right corner of the page. The vertical Z axis points upward such that the earth surface faces the top of the page. Material properties are listed in previous table for "granite" (blue) and "alluvium" (yellow). [Larry Murdoch, Milestone 5.1 of FORGE Project 3-2514]

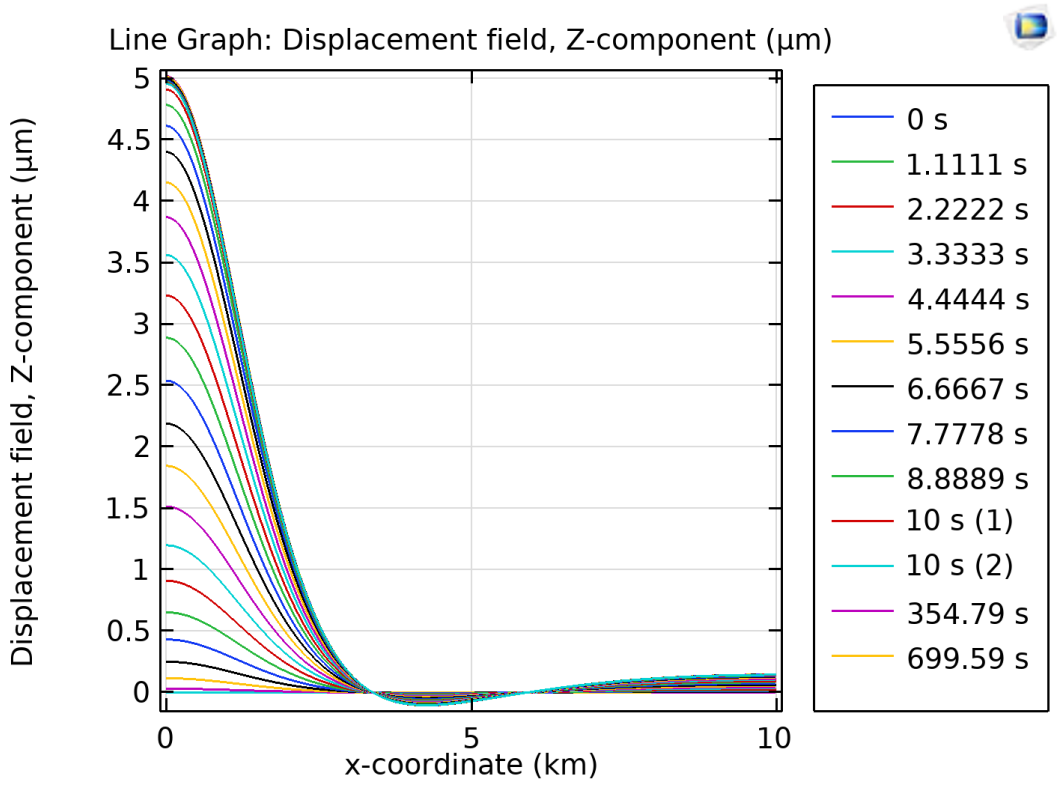

Figure 23. Simulated vertical displacement in micrometers at various times along a profile from west to east at Y=2 km.

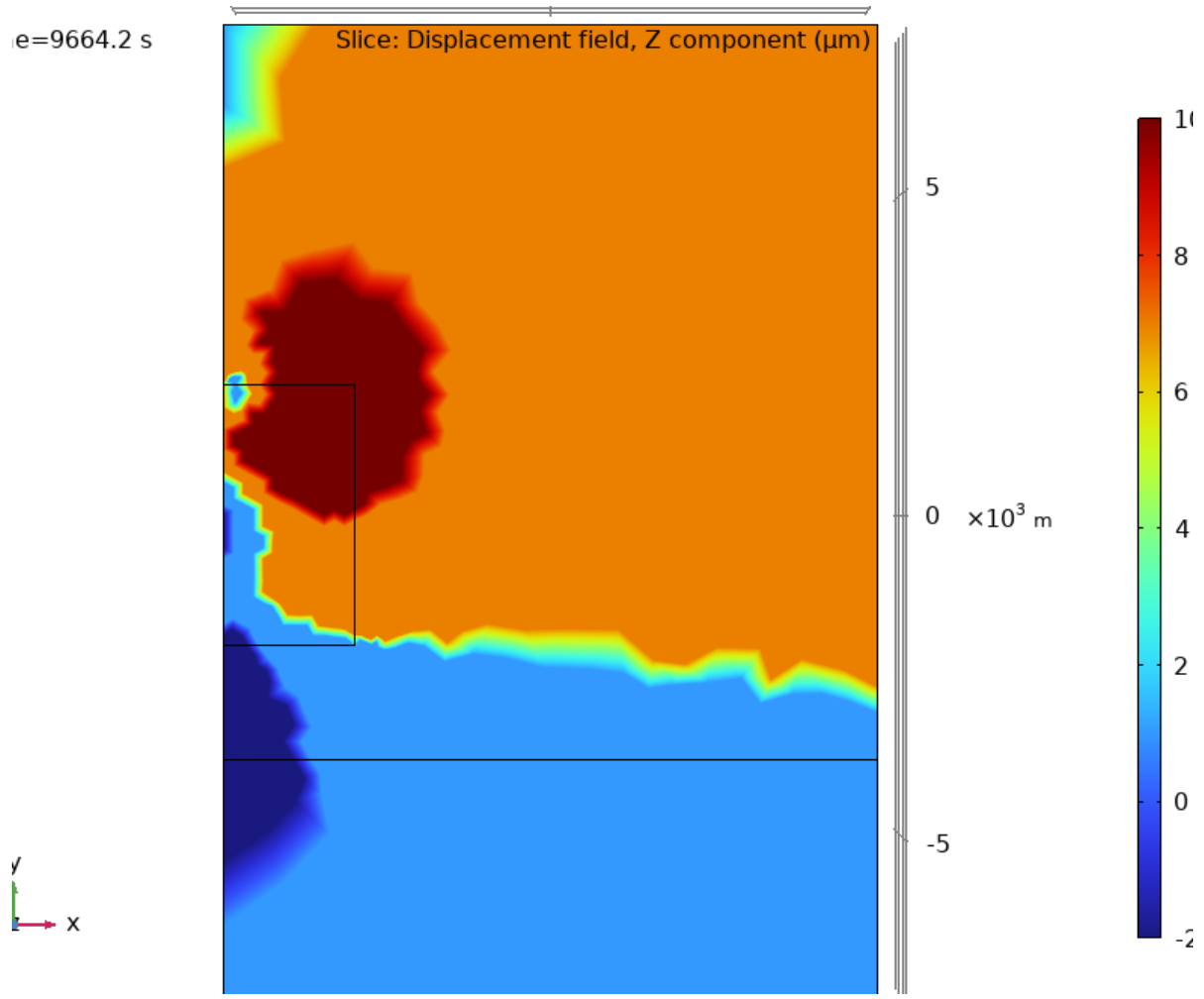

Figure 24. Map view of simulated vertical component of displacement in micrometers after approximately 2.5 hours of injection. Warm colors denote positive (upward) vertical displacement.

9 Supplementary Information

Table 4. List of SAR acquisitions from TerraSAR-X and TanDEM-X radar satellite missions showing date (YearMonthDate) and orbit number. The status flags are defined as follows: "D" represents a scene that has been delivered. "C" denotes a canceled scene acquisition, usually for technical reasons at the source. "P" denotes a scene that is planned for acquisition in the future. All of these acquisitions follow Track 30 in an ascending orbital pass that crosses the equatorial plane from south to north. Earlier acquisitions are listed in previous reports. [grep forge /s12/insar/TSX/TSX_OrderList.txt | cut -c 1-78 | sort -un]

#date	site	sat	track	swath	frame	orbit	ascdes	status	source
20161108	forge	TDX	T30	strip_004	nan	35404	A	D	dlrdlr
20181115	forge	TDX	T30	strip_004R	nan	46593	A	D	dlrdlr
20190131	forge	TSX	T30	strip_004R	nan	47762	A	D	dlrdlr
20190211	forge	TSX	T30	strip_004R	nan	47929	A	D	dlrdlr
20190222	forge	TSX	T30	strip_004R	nan	48096	A	D	dlrdlr
20190418	forge	TSX	T30	strip_004R	nan	48931	A	D	dlrdlr
20190510	forge	TSX	T30	strip_004R	nan	49265	A	D	dlrdlr
20190601	forge	TSX	T30	strip_004R	nan	49599	A	D	dlrdlr
20190623	forge	TSX	T30	strip_004R	nan	nan	A	C	dlrdlr
20190715	forge	TSX	T30	strip_004R	nan	nan	A	C	dlrdlr
20200107	forge	TSX	T30	strip_004R	nan	52939	A	D	dlrdlr
20200129	forge	TSX	T30	strip_004R	nan	53273	A	D	dlrdlr
20200220	forge	TSX	T30	strip_004R	nan	53607	A	D	dlrdlr
20200302	forge	TSX	T30	strip_004R	nan	53774	A	D	dlrdlr
20200313	forge	TSX	T30	strip_004R	nan	53941	A	D	dlrdlr
20200324	forge	TSX	T30	strip_004R	nan	54108	A	D	dlrdlr
20200404	forge	TSX	T30	strip_004R	nan	54275	A	D	dlrdlr
20200415	forge	TSX	T30	strip_004R	nan	54442	A	D	dlrdlr
20200426	forge	TSX	T30	strip_004R	nan	54609	A	D	dlrdlr
20200507	forge	TSX	T30	strip_004R	nan	54776	A	D	dlrdlr
20200518	forge	TSX	T30	strip_004R	nan	54943	A	D	dlrdlr
20200529	forge	TSX	T30	strip_004R	nan	55110	A	D	dlrdlr
20200609	forge	TSX	T30	strip_004R	nan	55277	A	D	dlrdlr
20200620	forge	TSX	T30	strip_004R	nan	55444	A	D	dlrdlr
20200701	forge	TSX	T30	strip_004R	nan	55611	A	D	dlrdlr
20200712	forge	TSX	T30	strip_004R	nan	55778	A	D	dlrdlr
20200723	forge	TSX	T30	strip_004R	nan	55945	A	D	dlrdlr
20200803	forge	TSX	T30	strip_004R	nan	56112	A	D	dlrdlr
20200814	forge	TSX	T30	strip_004R	nan	56279	A	D	dlrdlr
20200825	forge	TSX	T30	strip_004R	nan	56446	A	D	dlrdlr
20200905	forge	TSX	T30	strip_004R	nan	56613	A	D	dlrdlr
20200916	forge	TSX	T30	strip_004R	nan	56780	A	D	dlrdlr
20200927	forge	TSX	T30	strip_004R	nan	56947	A	D	dlrdlr
20201008	forge	TSX	T30	strip_004R	nan	57114	A	D	dlrdlr
20201019	forge	TSX	T30	strip_004R	nan	57281	A	D	dlrdlr
20201030	forge	TSX	T30	strip_004R	nan	57448	A	D	dlrdlr
20201110	forge	TSX	T30	strip_004R	nan	57615	A	D	dlrdlr
20201121	forge	TSX	T30	strip_004R	nan	57782	A	D	dlrdlr
20201202	forge	TSX	T30	strip_004R	nan	57949	A	D	dlrdlr
20201213	forge	TSX	T30	strip_004R	nan	58116	A	D	dlrdlr
20201224	forge	TSX	T30	strip_004R	nan	58283	A	D	dlrdlr
20210104	forge	TSX	T30	strip_004R	nan	58450	A	D	dlrdlr
20210115	forge	TSX	T30	strip_004R	nan	58617	A	D	dlrdlr
20210126	forge	TSX	T30	strip_004R	nan	58784	A	D	dlrdlr
20210206	forge	TSX	T30	strip_004R	nan	58951	A	D	dlrdlr
20210217	forge	TSX	T30	strip_004R	nan	59118	A	D	dlrdlr
20210228	forge	TSX	T30	strip_004R	nan	59285	A	D	dlrdlr
20210311	forge	TSX	T30	strip_004R	nan	59452	A	D	dlrdlr
20210322	forge	TSX	T30	strip_004R	nan	59619	A	D	dlrdlr
20210402	forge	TSX	T30	strip_004R	nan		A	C	dlrdlr
20210413	forge	TSX	T30	strip_004R	nan	59953	A	D	dlrdlr
20210424	forge	TSX	T30	strip_004R	nan	60120	A	D	dlrdlr
20210505	forge	TSX	T30	strip_004R	nan	60287	A	D	dlrdlr
20210516	forge	TSX	T30	strip_004R	nan	60454	A	D	dlrdlr
20210527	forge	TSX	T30	strip_004R	nan	60621	A	D	dlrdlr
20210607	forge	TSX	T30	strip_004R	nan		A	P	dlrdlr
20210618	forge	TSX	T30	strip_004R	nan		A	P	dlrdlr
20210629	forge	TSX	T30	strip_004R	nan	61122	A	D	dlrdlr
20210710	forge	TSX	T30	strip_004R	nan	61289	A	D	dlrdlr
20210721	forge	TSX	T30	strip_004R	nan	61456	A	D	dlrdlr
20210801	forge	TSX	T30	strip_004R	nan	61623	A	D	dlrdlr

20210812	forge	TSX	T30	strip_004R	nan	61790	A	D	dlrdlr
20210823	forge	TSX	T30	strip_004R	nan	61957	A	D	dlrdlr
20210903	forge	TSX	T30	strip_004R	nan	62124	A	D	dlrdlr
20210914	forge	TSX	T30	strip_004R	nan		A	C	
20210925	forge	TSX	T30	strip_004R	nan	62458	A	D	dlrdlr
20211006	forge	TSX	T30	strip_004R	nan	62625	A	D	dlrdlr
20211017	forge	TSX	T30	strip_004R	nan		A	C	dlrdlr
20211028	forge	TSX	T30	strip_004R	nan		A	C	dlrdlr
20211108	forge	TSX	T30	strip_004R	nan	63126	A	D	dlrdlr
20211119	forge	TSX	T30	strip_004R	nan	63293	A	D	dlrdlr
20211130	forge	TSX	T30	strip_004R	nan	63460	A	D	dlrdlr
20211211	forge	TSX	T30	strip_004R	nan	80357	A	D	dlrdlr
20211222	forge	TSX	T30	strip_004R	nan	80524	A	D	dlrdlr
20220102	forge	TSX	T30	strip_004R	nan	80691	A	D	dlrdlr
20220113	forge	TSX	T30	strip_004R	nan		A	C	dlrdlr
20220124	forge	TSX	T30	strip_004R	nan	81025	A	D	dlrdlr
20220204	forge	TSX	T30	strip_004R	nan	81192	A	D	dlrdlr
20220215	forge	TSX	T30	strip_004R	nan	81359	A	D	dlrdlr
20220226	forge	TSX	T30	strip_004R	nan	64796	A	D	dlrdlr
20220309	forge	TSX	T30	strip_004R	nan	64963	A	D	dlrdlr
20220320	forge	TSX	T30	strip_004R	nan	65130	A	D	dlrdlr
20220331	forge	TSX	T30	strip_004R	nan	65297	A	D	dlrdlr
20220411	forge	TSX	T30	strip_004R	nan	65464	A	D	dlrdlr
20220422	forge	TSX	T30	strip_004R	nan	65631	A	D	dlrdlr
20220503	forge	TSX	T30	strip_004R	nan	65798	A	D	dlrdlr
20220514	forge	TSX	T30	strip_004R	nan	65965	A	D	dlrdlr
20220525	forge	TSX	T30	strip_004R	nan	66132	A	D	dlrdlr
20220605	forge	TSX	T30	strip_004R	nan	66299	A	D	dlrdlr
20220616	forge	TSX	T30	strip_004R	nan		A	C	dlrdlr
20220627	forge	TSX	T30	strip_004R	nan	66633	A	D	dlrdlr
20220708	forge	TSX	T30	strip_004R	nan	66800	A	D	dlrdlr
20220719	forge	TSX	T30	strip_004R	nan	66967	A	D	dlrdlr
20220730	forge	TSX	T30	strip_004R	nan	67134	A	D	dlrdlr
20220810	forge	TSX	T30	strip_004R	nan	67301	A	D	dlrdlr
20220821	forge	TSX	T30	strip_004R	nan		A	C	dlrdlr
20220901	forge	TSX	T30	strip_004R	nan		A	C	dlrdlr
20220912	forge	TSX	T30	strip_004R	nan		A	C	dlrdlr
20220923	forge	TSX	T30	strip_004R	nan	67969	A	D	dlrdlr
20221004	forge	TSX	T30	strip_004R	nan		A	C	dlrdlr
20221015	forge	TSX	T30	strip_004R	nan	68303	A	D	dlrdlr
20221026	forge	TSX	T30	strip_004R	nan	68470	A	D	dlrdlr
20221106	forge	TSX	T30	strip_004R	nan	68637	A	D	dlrdlr
20221117	forge	TSX	T30	strip_004R	nan	68804	A	D	dlrdlr
20221128	forge	TSX	T30	strip_004R	nan	68971	A	D	dlrdlr
20221209	forge	TSX	T30	strip_004R	nan	69138	A	D	dlrdlr
20221220	forge	TSX	T30	strip_004R	nan	69305	A	D	dlrdlr
20221231	forge	TSX	T30	strip_004R	nan	69472	A	D	dlrdlr
20230111	forge	TSX	T30	strip_004R	nan	69639	A	D	dlrdlr
20230122	forge	TSX	T30	strip_004R	nan	69806	A	D	dlrdlr
20230202	forge	TSX	T30	strip_004R	nan	69973	A	D	dlrdlr
20230213	forge	TSX	T30	strip_004R	nan	70140	A	D	dlrdlr
20230224	forge	TSX	T30	strip_004R	nan	70307	A	D	dlrdlr
20230307	forge	TSX	T30	strip_004R	nan	70474	A	D	dlrdlr
20230318	forge	TSX	T30	strip_004R	nan	70641	A	D	dlrdlr
20230329	forge	TSX	T30	strip_004R	nan	70808	A	D	dlrdlr
20230409	forge	TSX	T30	strip_004R	nan	70975	A	D	dlrdlr
20230420	forge	TSX	T30	strip_004R	nan	71142	A	D	dlrdlr
20230501	forge	TSX	T30	strip_004R	nan	71309	A	D	dlrdlr
20230512	forge	TSX	T30	strip_004R	nan	71476	A	D	dlrdlr
20230523	forge	TSX	T30	strip_004R	nan	71643	A	D	dlrdlr
20230603	forge	TSX	T30	strip_004R	nan	71810	A	D	dlrdlr
20230614	forge	TSX	T30	strip_004R	nan	71977	A	D	dlrdlr
20230625	forge	TSX	T30	strip_004R	nan	72144	A	D	dlrdlr
20230706	forge	TSX	T30	strip_004R	nan	72311	A	D	dlrdlr
20230717	forge	TSX	T30	strip_004R	nan	72478	A	D	dlrdlr
20230728	forge	TSX	T30	strip_004R	nan	72645	A	D	dlrdlr
20230808	forge	TSX	T30	strip_004R	nan	72812	A	D	dlrdlr
20230819	forge	TSX	T30	strip_004R	nan	72979	A	D	dlrdlr
20230830	forge	TSX	T30	strip_004R	nan	73146	A	D	dlrdlr
20230910	forge	TSX	T30	strip_004R	nan	73313	A	D	dlrdlr
20230921	forge	TSX	T30	strip_004R	nan	73480	A	D	dlrdlr

20231002	forge	TSX	T30	strip_004R	nan		A	C	dlrdlr
20231013	forge	TSX	T30	strip_004R	nan	73814	A	D	dlrdlr
20231024	forge	TSX	T30	strip_004R	nan		A	C	dlrdlr
20231104	forge	TSX	T30	strip_004R	nan	74148	A	D	dlrdlr
20231115	forge	TSX	T30	strip_004R	nan	74315	A	D	dlrdlr
20231126	forge	TSX	T30	strip_004R	nan	74482	A	D	dlrdlr
20231207	forge	TSX	T30	strip_004R	nan	74649	A	D	dlrdlr
20231218	forge	TSX	T30	strip_004R	nan	74816	A	D	dlrdlr
20231229	forge	TSX	T30	strip_004R	nan	74983	A	D	dlrdlr
20240109	forge	TSX	T30	strip_004R	nan	75150	A	D	dlrdlr
20240120	forge	TSX	T30	strip_004R	nan	75317	A	D	dlrdlr
20240131	forge	TSX	T30	strip_004R	nan	75484	A	D	dlrdlr
20240211	forge	TSX	T30	strip_004R	nan	75651	A	D	dlrdlr
20240222	forge	TSX	T30	strip_004R	nan	75818	A	D	dlrdlr
20240304	forge	TSX	T30	strip_004R	nan	75985	A	D	dlrdlr
20240315	forge	TSX	T30	strip_004R	nan	76152	A	D	dlrdlr
20240326	forge	TSX	T30	strip_004R	nan	76319	A	D	dlrdlr
20240406	forge	TSX	T30	strip_004R	nan	76486	A	D	dlrdlr
20240417	forge	TSX	T30	strip_004R	nan	76653	A	D	dlrdlr
20240428	forge	TSX	T30	strip_004R	nan	76820	A	D	dlrdlr
20240509	forge	TSX	T30	strip_004R	nan	76987	A	D	dlrdlr
20240520	forge	TSX	T30	strip_004R	nan	77154	A	D	dlrdlr
20240531	forge	TSX	T30	strip_004R	nan	77321	A	D	dlrdlr
20240611	forge	TSX	T30	strip_004R	nan	77488	A	D	dlrdlr
20240622	forge	TSX	T30	strip_004R	nan	77655	A	D	dlrdlr

Table 5. List of interferometric pairs calculated by ASF HYP3 from data acquired by Sentinel-1A satellite mission showing spacecraft, date and time of first and second acquisitions, respectively. (hyp3-mintpy) [feigl@emidio SDK]$ find F -name "S1*unw_phase.tif" | tr '/' ',' | awk -F, '{print $4}' | tr I ',' | awk -F, '{print $1}' | sort -n | uniq*

SAT	YYYYMMDD_hhmmss	YYYYMMDD_hhmmss	polarization
S1AA	20200102T133453	20200114T133453	VVP012_
S1AA	20200114T133453	20200126T133452	VVP012_
S1AA	20200126T133452	20200207T133452	VVP012_
S1AA	20200207T133452	20200219T133452	VVP012_
S1AA	20200219T133452	20200302T133452	VVP012_
S1AA	20200302T133452	20200314T133452	VVP012_
S1AA	20200314T133452	20200326T133452	VVP012_
S1AA	20200326T133452	20200407T133452	VVP012_
S1AA	20200407T133452	20200419T133453	VVP012_
S1AA	20200419T133453	20200501T133453	VVP012_
S1AA	20200501T133453	20200513T133454	VVP012_
S1AA	20200513T133454	20200525T133455	VVP012_
S1AA	20200525T133455	20200606T133455	VVP012_
S1AA	20200630T133456	20200712T133457	VVP012_
S1AA	20200712T133457	20200724T133458	VVP012_
S1AA	20200724T133458	20200805T133459	VVP012_
S1AA	20200805T133459	20200817T133459	VVP012_
S1AA	20200817T133459	20200829T133500	VVP012_
S1AA	20200829T133500	20200910T133501	VVP012_
S1AA	20200910T133501	20200922T133501	VVP012_
S1AA	20200922T133501	20201004T133501	VVP012_
S1AA	20201004T133501	20201016T133502	VVP012_
S1AA	20201016T133502	20201028T133501	VVP012_
S1AA	20201028T133501	20201109T133501	VVP012_
S1AA	20201109T133501	20201121T133501	VVP012_
S1AA	20201121T133501	20201203T133501	VVP012_
S1AA	20201203T133501	20201215T133500	VVP012_
S1AA	20201215T133500	20201227T133500	VVP012_
S1AA	20201227T133500	20210108T133459	VVP012_
S1AA	20210108T133459	20210120T133458	VVP012_
S1AA	20210120T133458	20210201T133458	VVP012_
S1AA	20210201T133458	20210213T133458	VVP012_
S1AA	20210213T133458	20210225T133457	VVP012_
S1AA	20210225T133457	20210309T133457	VVP012_
S1AA	20210309T133457	20210321T133458	VVP012_
S1AA	20210321T133458	20210402T133458	VVP012_
S1AA	20210402T133458	20210414T133458	VVP012_
S1AA	20210414T133458	20210426T133459	VVP012_
S1AA	20210426T133459	20210508T133459	VVP012_
S1AA	20210508T133459	20210520T133500	VVP012_
S1AA	20210520T133500	20210601T133501	VVP012_
S1AA	20210601T133501	20210613T133502	VVP012_
S1AA	20210613T133502	20210625T133502	VVP012_
S1AA	20210625T133502	20210707T133503	VVP012_
S1AA	20210707T133503	20210719T133504	VVP012_
S1AA	20210719T133504	20210731T133504	VVP012_
S1AA	20210731T133504	20210812T133505	VVP012_
S1AA	20210812T133505	20210824T133506	VVP012_
S1AA	20210824T133506	20210905T133506	VVP012_
S1AA	20210905T133506	20210917T133507	VVP012_
S1AA	20210917T133507	20210929T133507	VVP012_
S1AA	20210929T133507	20211011T133507	VVP012_
S1AA	20211011T133507	20211023T133507	VVP012_
S1AA	20211023T133507	20211104T133507	VVP012_
S1AA	20211128T133506	20211210T133506	VVP012_
S1AA	20211210T133506	20211222T133505	VVP012_
S1AA	20211222T133505	20220103T133505	VVP012_
S1AA	20220103T133505	20220115T133504	VVP012_
S1AA	20220115T133504	20220127T133504	VVP012_
S1AA	20220127T133504	20220208T133503	VVP012_
S1AA	20220208T133503	20220220T133506	VVP012_
S1AA	20220220T133506	20220304T133506	VVP012_
S1AA	20220304T133506	20220316T133506	VVP012_
S1AA	20220316T133506	20220328T133506	VVP012_
S1AA	20220328T133506	20220409T133504	VVP012_

S1AA_20220409T133504_20220421T133504_VVP012_
S1AA_20220421T133504_20220503T133504_VVP012_
S1AA_20220503T133504_20220515T133506_VVP012_
S1AA_20220515T133506_20220527T133506_VVP012_
S1AA_20220527T133506_20220608T133507_VVP012_
S1AA_20220608T133507_20220620T133508_VVP012_
S1AA_20220620T133508_20220702T133509_VVP012_
S1AA_20220702T133509_20220714T133501_VVP012_
S1AA_20220714T133501_20220726T133502_VVP012_
S1AA_20220726T133502_20220807T133503_VVP012_
S1AA_20220807T133503_20220819T133503_VVP012_
S1AA_20220912T133505_20220924T133504_VVP012_
S1AA_20220924T133504_20221006T133505_VVP012_
S1AA_20221006T133505_20221018T133505_VVP012_
S1AA_20221018T133505_20221030T133505_VVP012_
S1AA_20221030T133505_20221111T133504_VVP012_
S1AA_20221111T133504_20221123T133505_VVP012_
S1AA_20221123T133505_20221205T133504_VVP012_
S1AA_20221205T133504_20221217T133503_VVP012_
S1AA_20221217T133503_20221229T133502_VVP012_
S1AA_20221229T133502_20230110T133502_VVP012_
S1AA_20230110T133502_20230122T133502_VVP012_
S1AA_20230122T133502_20230203T133501_VVP012_
S1AA_20230203T133501_20230215T133500_VVP012_
S1AA_20230215T133500_20230227T133501_VVP012_
S1AA_20230227T133501_20230311T133501_VVP012_
S1AA_20230311T133501_20230323T133501_VVP012_
S1AA_20230323T133501_20230404T133501_VVP012_
S1AA_20230404T133501_20230416T133501_VVP012_
S1AA_20230416T133501_20230428T133502_VVP012_
S1AA_20230428T133502_20230510T133502_VVP012_
S1AA_20230510T133502_20230522T133503_VVP012_
S1AA_20230522T133503_20230603T133504_VVP012_
S1AA_20230603T133504_20230615T133504_VVP012_
S1AA_20230615T133504_20230627T133505_VVP012_
S1AA_20230627T133505_20230709T133506_VVP012_
S1AA_20230709T133506_20230721T133507_VVP012_
S1AA_20230721T133507_20230802T133507_VVP012_
S1AA_20230802T133507_20230814T133508_VVP012_
S1AA_20230814T133508_20230826T133509_VVP012_
S1AA_20230826T133509_20230907T133509_VVP012_
S1AA_20230907T133509_20230919T133510_VVP012_
S1AA_20230919T133510_20231001T133510_VVP012_
S1AA_20231001T133510_20231013T133510_VVP012_
S1AA_20231013T133510_20231025T133510_VVP012_
S1AA_20231025T133510_20231106T133509_VVP012_
S1AA_20231106T133509_20231118T133509_VVP012_
S1AA_20231118T133509_20231130T133509_VVP012_
S1AA_20231130T133509_20231212T133509_VVP012_
S1AA_20231212T133509_20231224T133508_VVP012_
S1AA_20231224T133508_20240105T133507_VVP012_
S1AA_20240105T133507_20240117T133506_VVP012_
S1AA_20240117T133506_20240129T133506_VVP012_
S1AA_20240129T133506_20240210T133506_VVP012_
S1AA_20240210T133506_20240222T133506_VVP012_

Table 6. List of interferometric pairs calculated by ASF HYP3 from data acquired by Sentinel-1B satellite mission showing spacecraft, date and time of first and second acquisitions, respectively. (hyp3-mintpy) [feigl@emidio SDK]$ find F -name "S1*unw_phase.tif" | tr '/' ',' | awk -F, '{print $4}' | tr I ',' | awk -F, '{print $1}' | sort -n | uniq*

```
SAT  YYYYMMDD_hhmmss YYYYMMDD_hhmmss polarization
S1BB_20200103T012610_20200115T012610_VVP012_
S1BB_20200115T012610_20200127T012610_VVP012_
S1BB_20200127T012610_20200208T012609_VVP012_
S1BB_20200208T012609_20200220T012609_VVP012_
S1BB_20200220T012609_20200303T012609_VVP012_
S1BB_20200303T012609_20200315T012609_VVP012_
S1BB_20200315T012609_20200327T012609_VVP012_
S1BB_20200327T012609_20200408T012609_VVP012_
S1BB_20200408T012609_20200420T012610_VVP012_
S1BB_20200420T012610_20200502T012611_VVP012_
S1BB_20200502T012611_20200514T012611_VVP012_
S1BB_20200514T012611_20200526T012612_VVP012_
S1BB_20200526T012612_20200607T012613_VVP012_
S1BB_20200607T012613_20200619T012613_VVP012_
S1BB_20200619T012613_20200701T012614_VVP012_
S1BB_20200701T012614_20200713T012615_VVP012_
S1BB_20200713T012615_20200725T012615_VVP012_
S1BB_20200725T012615_20200806T012616_VVP012_
S1BB_20200806T012616_20200818T012617_VVP012_
S1BB_20200818T012617_20200830T012618_VVP012_
S1BB_20200830T012618_20200911T012618_VVP012_
S1BB_20200911T012618_20200923T012618_VVP012_
S1BB_20200923T012618_20201005T012619_VVP012_
S1BB_20201005T012619_20201017T012619_VVP012_
S1BB_20201017T012619_20201029T012619_VVP012_
S1BB_20201029T012619_20201110T012619_VVP012_
S1BB_20201110T012619_20201122T012618_VVP012_
S1BB_20201122T012618_20201204T012618_VVP012_
S1BB_20201204T012618_20201216T012617_VVP012_
S1BB_20201216T012617_20201228T012617_VVP012_
S1BB_20201228T012617_20210109T012616_VVP012_
S1BB_20210109T012616_20210121T012616_VVP012_
S1BB_20210121T012616_20210202T012615_VVP012_
S1BB_20210202T012615_20210214T012615_VVP012_
S1BB_20210214T012615_20210226T012615_VVP012_
S1BB_20210226T012615_20210310T012615_VVP012_
S1BB_20210310T012615_20210322T012615_VVP012_
S1BB_20210322T012615_20210403T012615_VVP012_
S1BB_20210403T012615_20210415T012616_VVP012_
S1BB_20210415T012616_20210427T012616_VVP012_
S1BB_20210427T012616_20210509T012617_VVP012_
S1BB_20210509T012617_20210521T012617_VVP012_
S1BB_20210521T012617_20210602T012618_VVP012_
S1BB_20210602T012618_20210614T012619_VVP012_
S1BB_20210614T012619_20210626T012620_VVP012_
S1BB_20210626T012620_20210708T012620_VVP012_
S1BB_20210708T012620_20210720T012621_VVP012_
S1BB_20210720T012621_20210801T012622_VVP012_
S1BB_20210801T012622_20210813T012622_VVP012_
S1BB_20210813T012622_20210825T012623_VVP012_
S1BB_20210825T012623_20210906T012624_VVP012_
S1BB_20210906T012624_20210918T012624_VVP012_
S1BB_20210918T012624_20210930T012624_VVP012_
S1BB_20210930T012624_20211012T012624_VVP012_
S1BB_20211012T012624_20211024T012625_VVP012_
S1BB_20211024T012625_20211105T012624_VVP012_
S1BB_20211105T012624_20211117T012624_VVP012_
S1BB_20211117T012624_20211129T012624_VVP012_
S1BB_20211129T012624_20211211T012623_VVP012_
S1BB_20211211T012623_20211223T012622_VVP012_
```